

INTRODUCTORY REVIEW ARTICLE

Cosmic Reionization

John H. Wise*

* Center for Relativistic Astrophysics, School of Physics, Georgia Institute of Technology, Atlanta, GA, USA

ARTICLE HISTORY

Compiled January 6, 2017

ABSTRACT

The universe goes through several phase transitions during its formative stages. Cosmic reionization is the last of them, where ultraviolet and X-ray radiation escape from the first generations of galaxies heating and ionizing their surroundings and subsequently the entire intergalactic medium. There is strong observational evidence that cosmic reionization ended approximately one billion years after the Big Bang, but there are still uncertainties that will be clarified with upcoming optical, infrared, and radio facilities in the next decade. This article gives an introduction to the theoretical and observational aspects of cosmic reionization and discusses their role in our understanding of early galaxy formation and cosmology.

KEYWORDS

cosmology; reionization; galaxy formation; first stars

1. Historical Preface

Astronomers use distant objects as flashlights to peer through the vast space between galaxies, the so-called intergalactic medium (IGM). Intervening gas clouds absorb light in particular atomic transitions, producing an absorption spectrum, which can then be used to study the evolution of IGM properties throughout cosmic time. The first quasi-stellar objects (known as QSOs or quasars) were identified in 1960 by Rudolph Minkowski¹ [1], Allan Sandage, and Maarten Schmidt [2]. They had star-like images, strong radio emission, and strangely placed, broad emission lines. Schmidt realized a few years later that the emission lines were actually hydrogen Balmer (principle quantum number $n \rightarrow 2$) series lines redshifted by 16% [3], who concluded that an extragalactic origin was the ‘most direct and least objectable’ explanation. This realization sparked a flurry of research on QSOs [e.g. 4–7], which were proposed to be powered by supermassive black holes (SMBHs) in 1964 by Edwin Salpeter [8] and Yakov Zel’dovich [9], and later associated with galactic nuclei by Donald Lynden-Bell [10] in 1969. These ideas were slowly accepted, but mounting evidence, especially with X-ray observations in the following decade [e.g. 11], confirmed the black hole paradigm.

Email: jwise@gatech.edu

¹Son of Hermann Minkowski of the ‘Minkowski spacetime’ in general relativity.

James Gunn and Bruce Peterson [12] first realized in 1965 that even if a tiny fraction ($\sim 10^{-4}$) of the IGM was neutral it would absorb the QSO light blueward of the Ly α wavelength at 1216 Å ($n = 1 \rightarrow 2$). However when interpreting the most distant QSO at the time (redshifted by a factor of 2.01), there was no such absorption, strongly suggesting that the IGM was *highly ionized* when the universe was only one-quarter of its present age of 13.8 billion years.

Cosmic reionization is the process in which the IGM becomes ionized and heated. Now from many observations of the IGM and early galaxies, we know that reionization² occurs everywhere in the IGM within a billion years after the Big Bang. As the first generations of galaxies fiercely form, they provide the necessary radiation to propel this cosmological event. Thus, it is informative to first overview some cosmological concepts and the astrophysics of photo-ionization in order to obtain a fuller understanding of reionization.

2. Background astrophysics

2.1. Cosmology

Cosmology is the study of the universe in its entirety. Large-scale galaxy surveys suggest that the universe follows the Cosmological Principle, stating the properties of the universe are the same for all observers when viewed at large enough scales (greater than 300 Mpc)³. In other words, the large-scale structure of the universe would be indistinguishable when traveling through space. At these scales, the universe is said to be *isotropic* and *homogeneous*. An isotropic universe means that there is no special direction in the universe, that is, it looks the same in all directions. A homogeneous universe is one with constant density and the distribution of galaxies is the same wherever the observer looks.

An isotropic and homogeneous universe can be treated as one entity. One can use general relativity to describe its dynamics, starting with the FLRW⁴ space-time metric,

$$ds^2 = c^2 dt^2 - a^2(t) \left(\frac{dr^2}{1 - Kr^2} + r^2 d\Omega^2 \right) \quad (1)$$

which results in an equation of motion describing its expansion or contraction. Here ds , dt , and $d\Omega$ are intervals of space-time, time, and angle, respectively, and c is the speed of light. The variable r is a spherical coordinate describing some observer and not necessarily a distance measure between two observers. The curvature K is a constant and can be either -1 , 0 , or $+1$, respectively corresponding to negative (elliptical), flat (Euclidean), and positive (hyperbolic) curvature of space.

The scale factor $a(t)$ denotes the expansion of the universe, where it is convention to take $a = 1$ at the present day. In other words, when the universe had only expanded to half of its current size, $a = 1/2$. The scale factor is also related to cosmological redshift $z = 1/a - 1$, which is common measure of distance and time in

²In this article, we refer to ‘reionization’ as the reionization of hydrogen and singly-ionized helium. Helium is doubly-ionized at a time 2–3 billion years after the Big Bang.

³1 Mpc = 3.26 million light-years = 3.086×10^{24} cm

⁴Friedmann-Lemaître-Robertson-Walker, all of who independently formulated this metric in the 1920’s and 1930’s.

cosmology. A solution to the FLRW metric is the Friedmann equation

$$\left(\frac{\dot{a}}{a}\right)^2 = H^2(t) = \frac{8\pi G}{3}\rho - \frac{Kc^2}{a^2}, \quad (2)$$

where $H(t)$ is the Hubble parameter, describing the expansion or contraction rate of the universe. The total mass-energy density $\rho = \rho_m + \rho_r + \rho_\Lambda$ of the universe comprises

- non-relativistic (cold) matter ($\rho_m \propto a^{-3}$) being geometrically diluted as space expands,
- radiation ($\rho_r \propto a^{-4}$) being both geometrically diluted and softened as its frequency is cosmologically redshifted, and
- vacuum energy, the so-called cosmological constant or dark energy, ($\rho_\Lambda \propto a^0$) that is pervasive and uniform throughout the universe.

Current constraints on the mass-energy components come from several experiments and sources—cosmic microwave background, supernovae, galaxy clusters, and large-scale structure. They have shown that the universe is flat ($K = 0$), and about 69%, 26%, and 5% of the mass-energy is contained in dark energy, cold dark matter (DM), and baryons, respectively [13]. A small fraction (9.25×10^{-5}) is contained in radiation. These percentages are always given in units of the critical density $\rho_c = 3H_0^2/8\pi G$: $(\Omega_\Lambda, \Omega_c, \Omega_b, \Omega_r) \simeq (0.69, 0.26, 0.05, 9.25 \times 10^{-5})$. Unless otherwise stated, we assume these cosmological parameters in this article.

The Friedmann equation can be integrated to find that the scale factor a is proportional to $t^{1/2}$ in a radiation-dominated universe, $t^{2/3}$ in a flat matter-dominated (the so-called Einstein-de Sitter, EdS) universe, and expands exponentially in a vacuum-dominated universe. The latest observational constraints suggest that the universe is flat and the cosmological constant exists ($\rho_\Lambda > 0$), thus the scale factor $a(t)$ is monotonically increases with time, i.e. the universe is expanding and accelerating.

Knowing how the universe expands as a function of time, we also know how the mean temperature of the universe behaves, assuming it is filled with a perfect fluid. Starting from a hot Big Bang, the universe undergoes several phase transitions; some are associated with the splitting of the four fundamental forces: gravity, strong, weak, and electromagnetic. Throughout these phase transitions, density perturbations steadily grow through gravitational instability, which eventually form galaxies. They are seeded by quantum fluctuations that exponentially grew in size during the inflationary epoch ($t \sim 10^{-36} - 10^{-32}$ s after the Big Bang) to macroscopic entities.

Furthermore, the production of elementary particles depends on the thermal history of the universe. As the universe expands and cools, particles ‘freeze-out’ from a coupled photon-particle fluid. For example when the temperature is greater than 0.511 MeV ($T = 5.8 \times 10^9$ K), electron-positron pairs are produced through pair production, $\gamma + \gamma \leftrightarrow e^- + e^+$, which also creates electronic neutrinos, $e^- + e^+ \leftrightarrow \nu_e + \bar{\nu}_e$. These particles and photons are all in thermal equilibrium when the temperature is much greater than their rest mass energy. Once the temperature drops below this value, the particles freeze-out and retain the distribution function that the particle population had at the time of freeze-out.

We start at the beginning of the quark epoch when the electroweak force split into the familiar electromagnetic and weak forces. This occurs only 10^{-12} seconds after the Big Bang when the temperatures $T \sim 10^{20}$ K ($E = k_B T \sim 10^{16}$ eV, where k_B is the Boltzmann constant), preventing quarks from binding into hadrons. The

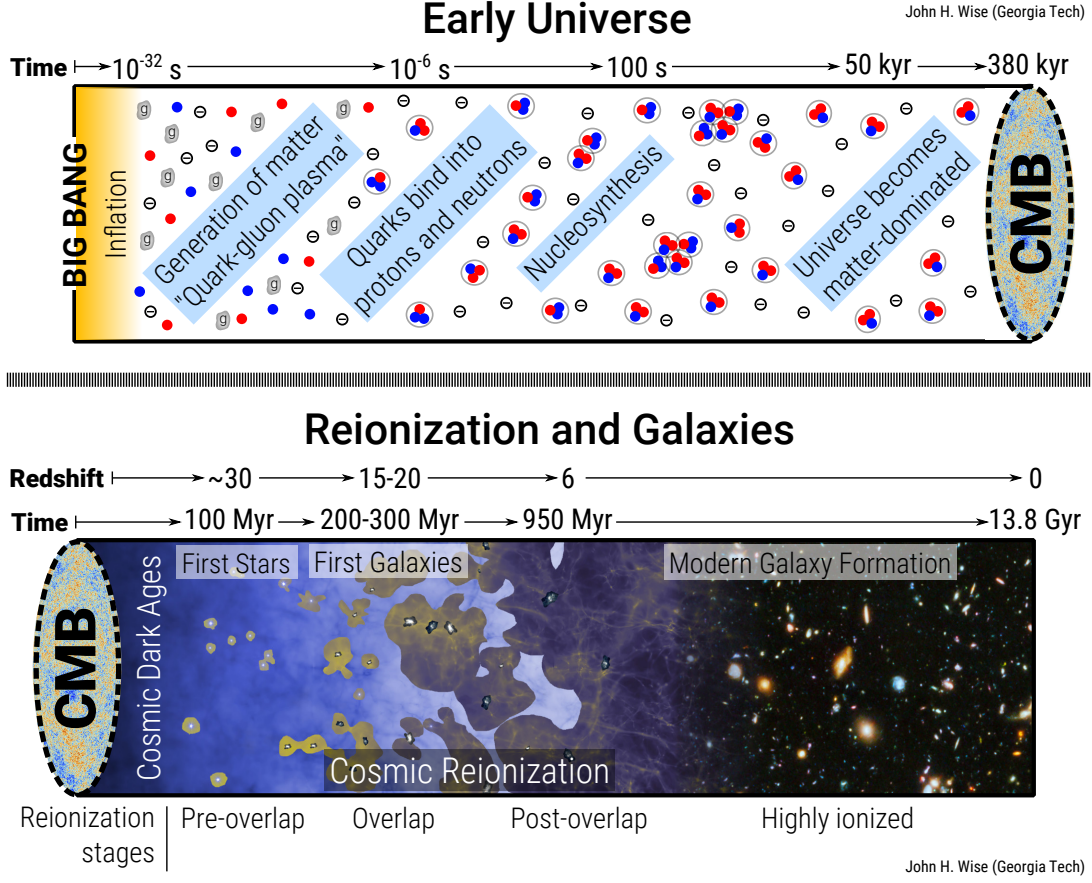


Figure 1. Cosmic timeline of the universe before (top) and after (bottom) recombination along with the stages of reionization. The galaxy survey image is taken from the *Hubble Ultra Deep Field*.

universe was filled with quarks, gluons, leptons, and photons, otherwise known as a 'quark-gluon plasma'. As the universe cooled, the following particle production (phase transitions) events occurred, which are also shown in Figure 1.

- $T \sim 10^{13}$ K ($t \sim 10^{-6}$ s): Quarks bind together to form hadrons. Afterwards, the universe is composed of relativistic pion, nucleons, charged leptons, and their associated neutrinos.
- $T \sim 10^{12}$ K ($t \sim 10^{-4}$ s): The charged pions annihilate while the neutral pions decay into photons. The only hadrons left are neutrons and protons.
- $T \sim 10^{11}$ K ($t \sim 10^{-2}$ s): Neutrons start to become less frequent than protons through weak interactions due to the neutron being slightly more massive than the proton with $\Delta mc^2 \approx 1.3$ MeV.
- $T \sim 5 \times 10^9$ K ($t \sim 4$ s): Annihilations of electron and positron pairs begin, which had facilitated the weak interactions between neutrons and protons. The neutron-to-proton ratio freezes out at $\exp(-\Delta mc^2/k_B T) \sim 1/10$.
- $T \sim 10^9$ K ($t \sim \text{few min}$): Nucleosynthesis starts, creating hydrogen, deuterium, helium, and lithium. All elements are *ionized*.
- $T \sim 4000$ K ($t \simeq 3.8 \times 10^5$ yr; $z \simeq 1090$): Recombination of electrons and nuclei, known as the surface of last scattering. Because the free electron density decreases, the photons become decoupled and stream away, creating the cosmic microwave background (CMB) and leaving the universe *neutral and still cooling*.

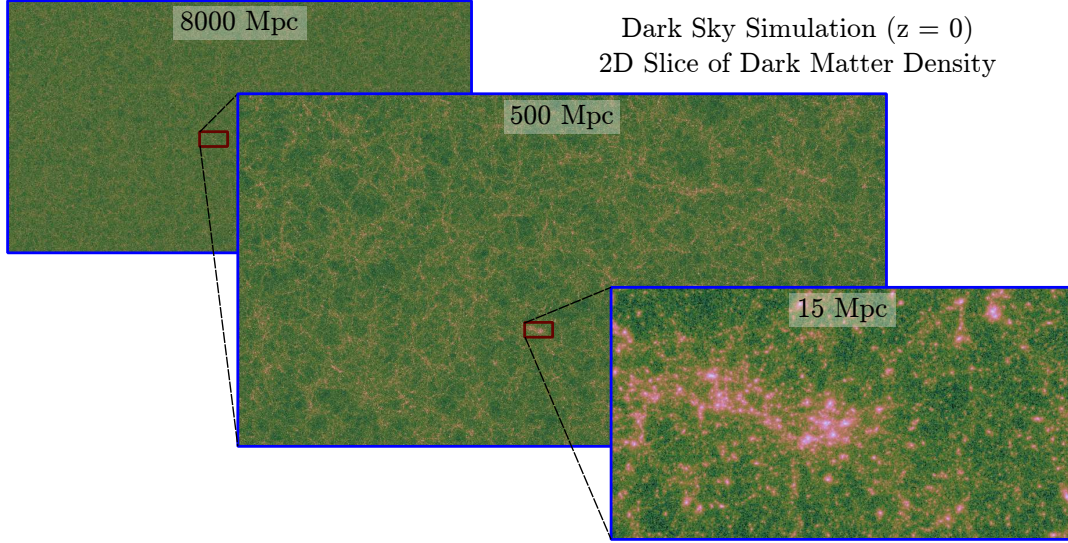


Figure 2. The Cosmic Web shown through slices of dark matter density in the Dark Sky Simulations [15] at the present-day. The fields of view in the left, center, and right panels are 8000, 500, and 15 Mpc. The universe is homogeneous and isotropic at scales above 300 Mpc but below which forms large-scale structures (clusters, filaments, walls, and voids).

After photons decouple, the universe at this time is a very dark and lonely place before stars or galaxies have formed. This epoch is sometimes referred to as the ‘Dark Ages’ [14]. From this starless, neutral, and cold state, the entire universe will be gradually reionized by nascent galaxies and their constituents.

2.2. Large-Scale Structure

On small scales, the universe is neither isotropic nor homogeneous. One can look at our Milky Way and other galaxies just to see the inhomogeneity of matter. In the absence of light pollution, the dense stellar fields of the Milky Way, intertwined with dark dust lanes, stretch from horizon to horizon. Our galaxy is a very clumpy and active region in the universe, scattered with stellar clusters, cold molecular clouds, warm ionized regions, and hot supernova remnants.

On slightly larger scales, these ‘island universes’ congregate in groups and clusters, containing dozens and hundreds of galaxies, respectively, which are connected to each other through long filaments. These cosmic connections form the cosmic web (see Figure 2) containing all cosmic structure: groups, clusters, superclusters, filaments, walls, and voids. When viewed in hundreds of Mpc, galaxy number densities become uniform, and web seems to repeat itself, suggesting the Cosmic Principle holds.

The cold dark matter (CDM) paradigm [16–18] explains cosmological large-scale structure extremely well, predicting galaxy number densities and their clustering to great accuracy. Because DM consists of the most of the matter, it controls the dynamics of large-scale structure. In any CDM cosmology, the building blocks are DM halos that have gravitationally collapsed and decoupled from the expansion of the universe. When a halo collapses, the dark matter and gas reaches virial equilibrium through violent relaxation (phase mixing) [19] as it balances its gravitational energy with twice its thermal and kinetic energy. As the halo virializes, it reaches a mean

overdensity of $18\pi^2 \approx 178$ with respect to the critical density ρ_c . However, it is customary to define a DM halo with mass M_{vir} as a sphere with a mean overdensity of $200\rho_c$, resulting in the following definitions for the virial radius r_{vir} , circular velocity V_c , and virial temperature T_{vir} ,

$$r_{\text{vir}} = \left[\frac{GM_{\text{vir}}}{100H(z)} \right]^{1/3}, \quad V_c = \sqrt{\frac{GM_{\text{vir}}}{r_{\text{vir}}}}, \quad T_{\text{vir}} = \frac{\mu m_p V_c^2}{2k_B}. \quad (3)$$

Here the Hubble parameter for a flat universe

$$H(z) = H_0 E(z); \quad E(z) \equiv (\Omega_{\Lambda,0} + \Omega_{m,0}(1+z)^3 + \Omega_{r,0}(1+z)^4)^{1/2} \quad (4)$$

is evaluated at some redshift z ; the mean molecular weight $\mu = (0.6, 1.22)$ for an ionized and neutral primordial gas, respectively, in units of the proton mass m_p . The 0-subscripts indicate that the variables are the present-day values.

CDM structure forms hierarchically with objects growing through a series of halo mergers. Galaxies exist at the centers of DM halos and are along for the ride throughout mergers, sparking galaxy interactions and mergers. The frequency of DM halos can be calculated through Press-Schechter formalism [20] and its ellipsoidal counterpart [21] that have been calibrated with numerical simulations [22]. This formalism asserts that the cosmic web grows *self-similarly*, in that, its structural properties remain the same as its characteristic mass increases with time. For instance, a present-day density distribution shown in Figure 2 could easily be representative of a scale dozens of times smaller at redshift $z = 15$ when the universe was only 250 Myr old.

All galaxies are seeded from the quantum fluctuations during the inflationary epoch ($t \sim 10^{-36} - 10^{-32}$ s). These models predict the perturbations to have Gaussian random statistics, where the overdensity ($\delta \equiv \rho/\bar{\rho} - 1$) distribution follows a zero-mean Gaussian one. If large-scale structure and halos grow self-similarly, Gaussian random statistics hold throughout time at large scales. One can imagine randomly placing spheres of radius R in the universe and measuring the mass variance $\sigma^2(R)$. The variance depends on the power spectrum of density perturbations and the scale R (or equivalently $M \equiv (4\pi/3)\bar{\rho}R^3$) and fully describes the zero-mean overdensity distribution. The collapsed mass fraction f_c can be calculated from this distribution by determining a critical overdensity δ_c in which objects will collapse and virialize to form a bound DM halo.

To answer this question, we turn to linear perturbation theory that accurately describes the early density evolution. It is beneficial to use the overdensity δ_0 *linearly extrapolated* to the present-day as a proxy to the actual overdensity in the non-linear regime. A spherical collapse model [23] predicts the halo will collapse to a point when $\delta_0 \simeq 1.69$. In reality, any deviation from spherical symmetry and phase mixing will prevent the halo from collapsing to a singularity. To generalize δ_0 to any redshift z , we have to divide out the growth factor

$$D(z) = \frac{g(z)}{g(0)(1+z)} \quad (5)$$

with

$$g(z) \approx \frac{5}{2}\Omega_m \left[\Omega_m^{4/7} - \Omega_\Lambda + (1 + \Omega_m/2)(1 + \Omega_\Lambda/70) \right]^{-1} \quad (6)$$

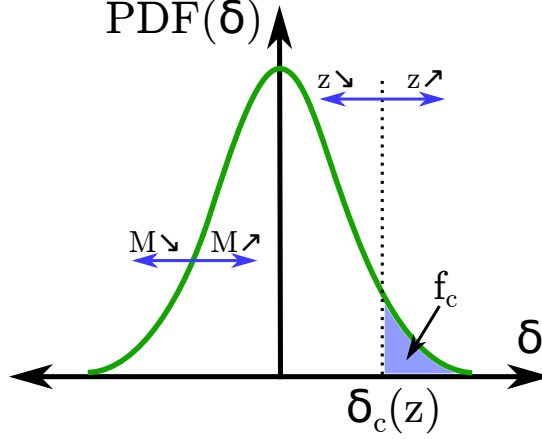


Figure 3. The probability distribution function of Gaussian random overdensities δ . The distribution becomes wider (narrower) with decreasing (increasing) halo mass M . The collapsed mass fraction f_c in Press-Schechter formalism [20] is the mass that exceeds the critical overdensity δ_c for gravitational collapse. This barrier to collapse increases with redshift.

that describes how a linear overdensity grows, normalized to unity at the present-day [24]. Here mass-energy fractions are given at redshift z and are related to their present-day values by

$$\Omega_m = \frac{\Omega_{m,0}(1+z)^3}{E^2(z)} \quad \text{and} \quad \Omega_\Lambda = \frac{\Omega_{\Lambda,0}}{E^2(z)} \quad (7)$$

with $E(z)$ given in Equation (4). This gives a critical overdensity $\delta_c \equiv \delta_0/D(z)$. Now for given halo mass M and redshift z , the collapsed fraction f_c is simply the complementary error function of a Gaussian distribution with $\sigma(M)$, evaluated at δ_c , illustrated in Figure 3. This is usually expressed as

$$f_c(> M, z) = \text{erfc} \left(\frac{\nu}{\sqrt{2}} \right) \quad (8)$$

with $\nu \equiv \delta_0/[D(z)\sigma(M)]$. It is commonplace to call halos ν - σ (i.e. 1 - σ) halos to describe the rarity and/or mass at some redshift. The number density n of halos in the mass range $M \rightarrow M + dM$ is calculated by differentiating Equation (8) with respect to mass, obtaining

$$n(M, z) dM = \sqrt{\frac{2}{\pi}} \frac{\bar{\rho}_0}{M} \left| \frac{d\nu}{dM} \right| \exp \left(-\frac{\nu^2}{2} \right) dM, \quad (9)$$

which is known as the Press-Schechter (PS) mass function.

Armed with PS formalism, we can now ask the questions: *How frequently do stars and galaxies form in the early universe, and generally when do they form?* For a halo to host star formation, the gas must be able to cool and condense through radiative cooling. Catastrophic cooling and collapse occurs when a halo reaches some critical mass. With this mass, we can estimate the abundance of the first stars and galaxies as a function of time. Their radiation will permeate the IGM, photoionizing and photo-heating it. To study reionization from first principles point of view, we next overview the basic physics of photo-ionization.

2.3. Ionization and recombination

The radiation from the first luminous objects will ionize and heat the surrounding IGM once it escapes from their host halos. These are known as cosmological H II regions. The ionization and recombination of hydrogen atoms ($\text{H} + \gamma \leftrightarrow \text{H}^+ + \text{e}^-$) are dominant processes in H II regions. Ionizations occur when photons with energies $E > I_{\text{H}} = 13.6 \text{ eV}$ interact with neutral hydrogen atoms, where their excess energies are subsequently thermalized. Recombinations occur when the Coulomb force attracts protons and electrons, which becomes efficient at temperatures $T \leq 10^4 \text{ K}$. One recombination releases a photon with an energy that is the sum of the kinetic energy of the electron and binding energy of the quantum state, I_{H}/n^2 . If the electron recombines into an excited state ($n > 1$), the electron will quickly decay into the ground state in a series of transitions.

In a region with ionizing radiation, the gas approaches ionization balance with the recombination rate equaling the ionization rate. To calculate the recombination rate, we can make the following assumptions: (i) the rate will be proportional to the number density of protons n_{p} and electrons n_{e} , (ii) the gas is pure hydrogen, giving $n_{\text{p}} = n_{\text{e}}$, and (iii) the rate depends on the temperature and into which quantum state n it recombines. Thus, we can write the recombination rate *per unit volume* into level n as

$$\dot{\mathcal{N}}_{\text{n}} = n_{\text{e}}n_{\text{p}}\alpha_{\text{n}}(T) = n_{\text{e}}^2\alpha_{\text{n}}(T) \text{ m}^{-3} \text{ s}^{-1}, \quad (10)$$

where α_{n} is the recombination rate coefficient into level n . The total recombination rate, known as 'case A', is the sum of recombination rates into all levels. However if an electron recombines directly into the ground state, this will release a photon that can ionize another hydrogen atom, which is not the case if it recombines into an excited state. Effectively, there are zero net recombinations in this case, and we can ignore the $n = 1$ recombination rate. The total recombination rate into excited states, known as the 'on-the-spot' or 'case B' approximation, is

$$\dot{\mathcal{N}}_{\text{R}} = \sum_{n=2}^{\infty} \dot{\mathcal{N}}_{\text{n}} \equiv n_{\text{e}}^2\alpha_{\text{B}}(T) \text{ m}^{-3} \text{ s}^{-1}, \quad (11)$$

where

$$\alpha_{\text{B}}(T) \approx 2.59 \times 10^{-13} \left(\frac{T}{10^4 \text{ K}} \right)^{-0.845} \text{ cm}^3 \text{ s}^{-1} \quad (12)$$

is the case B recombination rate coefficient [25].

The ionization rate can be calculated given some ionizing radiation flux F in units of photons per second per unit area. Photons will be absorbed as they travel through a medium with a neutral hydrogen number density n_{HI} , and the probability for a single absorption is quantified by the photoionization cross-section $\sigma_{\text{HI}} \approx 6.8 \times 10^{-18} (E/13.6 \text{ eV})^{-3} \text{ cm}^2$ that decreases with photon energy. The cross-section is zero below 13.6 eV because the photon does not have sufficient energy to ionize hydrogen. Given these quantities, the ionization rate

$$\dot{\mathcal{N}}_{\text{I}} = \sigma_{\text{HI}}n_{\text{HI}}F \text{ cm}^{-3} \text{ s}^{-1}. \quad (13)$$

In ionization equilibrium, the recombination rate equals the ionization rate, giving

$$x_e^2 n^2 \alpha_B(T) = \sigma_{\text{HI}}(1 - x_e) n_H F, \quad (14)$$

where $x_e \equiv n_e/n_H$ is the ionization fraction and n_H is the total hydrogen number density. Solving for the ionization fraction and using the inverse square-law ($F = \dot{N}_\gamma/4\pi r^2$, where \dot{N}_γ is the ionizing photon luminosity), we can solve for x_e

$$\frac{x_e^2}{1 - x_e} = \frac{\dot{N}_\gamma}{4\pi r^2 n_H} \frac{\sigma_{\text{HI}}}{\alpha_B(T)} = 2.9 \times 10^4 \left(\frac{r}{1 \text{ pc}} \right)^{-2} \left(\frac{\dot{N}_\gamma}{10^{49} \text{ s}^{-1}} \right) \quad (15)$$

with $n_H = 100 \text{ cm}^{-3}$, $E = 13.6 \text{ eV}$, and $T = 10^4 \text{ K}$. The H II region is *highly ionized*, $x_e \approx 1$, and in this limit, we can approximate

$$x_e \approx 1 - 3.45 \times 10^{-5} \left(\frac{r}{1 \text{ pc}} \right)^2 \left(\frac{\dot{N}_\gamma}{10^{49} \text{ s}^{-1}} \right)^{-1}, \quad (16)$$

showing that H II regions are well described with a fully ionized plasma.

2.4. Properties of H II regions

A radiation source can only provide a finite number of ionizing photons per second, so there must be some limit of ionizations possible in the surrounding region. Recombinations are happening concurrently with ionizations in the highly ionized H II region. In some radial direction, if all of the ionizing photons are absorbed by newly recombined atoms inside the H II region, there will be no more flux left at the ionization front. When this happens, the front stalls out and reaches an equilibrium [26]. We can determine the radius R_s , known as the Strömgren radius, by balancing the total number of ionizations and recombinations in a region. Assuming spherical symmetry and a static and uniform medium, we set these total numbers to be equal,

$$V_{\text{sphere}} \dot{N}_R = \frac{4}{3} \pi R_s^3 (x_e n_H)^2 \alpha_B(T) = \dot{N}_\gamma. \quad (17)$$

Taking $x_e = 1$ and solving for R_s , we obtain

$$R_s = \left[\frac{3 \dot{N}_\gamma}{4 \pi n_H^2 \alpha_B(T)} \right]^{1/3} \quad (18)$$

$$\approx 3.44 \left(\frac{n_H}{100 \text{ cm}^{-3}} \right)^{-2/3} \left(\frac{\dot{N}_\gamma}{10^{49} \text{ s}^{-1}} \right)^{1/3} \left(\frac{T}{10^4 \text{ K}} \right)^{-0.282} \text{ pc} \quad (19)$$

This calculation can also be generalized to a power-law density profile $n_H(r) = n_{H,0}(r/r_0)^{-\beta}$.

Besides very close to the radiation source, ionization fronts do not travel at the speed of light. Recombinations in the H II region consume the ionizing photons that would otherwise reach the ionization front. We can estimate the speed of the ionization front by considering a photon flux F and assuming that every photon results

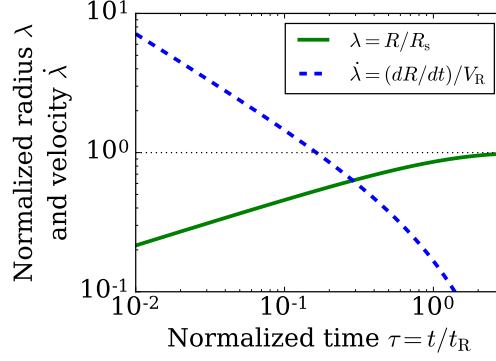


Figure 4. Evolution of the normalized radius λ and velocity $\dot{\lambda}$ of an isolated H II region in a uniform medium. The time is normalized to the recombination time t_R ; the radius is normalized to the Strömgren radius R_s , and the velocity is normalized to $V_R \equiv R_s/t_R$. The H II region requires a few recombination times to reach an equilibrium and slows dramatically as recombinations in the interior consume photons before reaching the ionization front.

in one ionization (i.e. no recombinations in the front). Here we will assume that the ambient medium has a uniform number density $n_{H,0}$, and the following analysis is similar for a radial density power-law profile. In the shell that bounds the H II region, we can equate the number of photons impacting a unit area in some time dt and the neutral column density in a shell of thickness dR , $F dt = n_{H,0} dR$, giving the ionization front speed

$$\frac{dR}{dt} = \frac{F}{n_{H,0}}. \quad (20)$$

Now we need to calculate the flux F by considering the spherical dilution of the radiation and recombinations within the H II region. The total incident radiation on the ionization front must be equal to the stellar output minus any photons lost in recombinations. Thus, we can write the following ionization balance equation,

$$\dot{N}_\gamma = 4\pi R^2 F + \frac{4}{3}\pi R^3 n_{H,0}^2 \alpha_B. \quad (21)$$

Solving for F and inserting it into Equation (20), we obtain

$$\frac{dR}{dt} = \frac{\dot{N}_\gamma}{4\pi R^2 n_{H,0}} - \frac{1}{3} R n_{H,0} \alpha_B. \quad (22)$$

We can solve this equation by relating the radius to the Strömgren radius R_s for a uniform medium (Equation 18) and the time to the recombination time $t_R = 1/(n_{H,0}\alpha_B)$. We make the Equation (22) dimensionless

$$\dot{\lambda} \equiv \frac{d\lambda}{d\tau} = \frac{1}{3\lambda^2} (1 - \lambda^3) \quad (23)$$

by defining the following variables: $\lambda \equiv R/R_s$, $\tau \equiv t/t_R$, $V_R \equiv R_s/t_R$, and $\dot{\lambda} \equiv d\lambda/d\tau = (dR/dt)/V_R$. This equation has the solution

$$\lambda \equiv \frac{R}{R_s} = (1 - e^{-\tau})^{1/3} \quad (24)$$

and its time-like derivative is

$$\dot{\lambda} \equiv \frac{dR}{dt} \frac{t_R}{R_s} = \frac{e^{-\tau}}{3} (1 - e^{-\tau})^{-2/3} \quad (25)$$

Figure 4 shows the evolution of λ and $\dot{\lambda}$ up to three recombination times. To give some example values, an ionization front traveling through a neutral medium with $n_{H,0} = 100 \text{ cm}^{-3}$ has a velocity of 2630 km s^{-1} at a radius $R = 0.46R_s$ and time $t = 0.1t_R$, and slows down to 300 km s^{-1} at a radius $R = 0.86R_s$ after one recombination time.

When Strömgren [26], and later Spitzer [27] for a dynamical system, derived these expressions, individual stars and stellar clusters were the target. But they can easily be applied to entire galaxies in a cosmological context [28, 29], where \dot{N}_γ is the ionizing photon luminosity that actually *escapes* into the IGM.

3. Ending the Cosmic Dark Ages

Cosmic reionization involves the coupling of non-linear physics of galaxy formation with the non-local physics of gravity and radiation transport to produce a global phase transition. Reionization is completely different from the local nature of the earlier phase transitions that only depend on the thermal state of the plasma. The mixture of small- and large-scale physics makes for a complex problem. Some important questions to ask about cosmic reionization are: *What are the main sources of reionization? When does reionization begin and end? What is the topology of the ionized regions? What can be learned about early galaxies from reionization and vice-versa? How does reionization affect galaxy formation?*

The present-day IGM has a mean temperature around 10^5 K and the primordial elements of hydrogen and helium are near complete ionization [e.g. 30]. Maintaining this relatively high temperature and ionization state is an ultraviolet and X-ray radiation background, sourced by countless galaxies and their central black holes [31]. But how did the IGM become ionized and heated in the first place? This becomes a particularly rich question when combined with the fact that galaxies were first assembling during the epoch of reionization (EoR).

Cosmic reionization can be divided into three phases [32]—pre-overlap, overlap, and post-overlap—that describe the connectivity of the cosmological H II regions, illustrated in Figure 1. In the pre-overlap phase, each galaxy produces its own H II region as it forms. These regions are divided by a vast neutral IGM, and their evolution can be treated independently, only requiring the escaping ionizing luminosity of the central galaxy. In the overlap phase, these regions start to combine with nearby regions [33]. Multiple galaxies can contribute to the UV emissivity that pervades the ionized region, dramatically increasing the mean free path of ionizing photons and accelerating the reionization process. Finally in the post-overlap phase, most of the IGM is ionized with some neutral patches remaining the universe. These neutral regions erode away as ionization fronts created from the UVB propagate into these vestiges of an earlier cosmic time.

3.1. The Dark Ages

The Cosmic Dark Ages began after recombination at $z \sim 1090$ and lasted until the first stars and galaxies started to light up the universe hundreds of millions of years later. However first, it is worthwhile to discuss the supersonic relative velocities between DM and gas that arises before and during recombination. The importance of this phenomenon was overlooked until recently [34], where the free electrons scatter off photons, strongly coupling the gas and radiation, but the collisionless DM is not affected by this coupling. These two components of the universe thus had different velocities as radiation and gas decoupled at recombination. The root-mean-square value at this time was $\sim 30 \text{ km s}^{-1}$ and fluctuated on comoving scales between $\sim 3 - 200 \text{ Mpc}$. Thus on comoving scales of $\sim \text{Mpc}$, the gas has a uniform bulk velocity relative to DM. This so-called streaming velocity decayed as a^{-1} , remained supersonic throughout the Dark Ages, and prevented gas from collecting in the potential wells of the smallest DM halos that would have otherwise formed stars.

The mean gas temperature of the universe after recombination is tightly coupled to the CMB temperature through Compton scattering until a redshift $z_t \approx 136$ at which time $T = 2.73 \text{ K}(1 + z_t) = 374 \text{ K}$ [35]. Afterwards in the absence of any heating, the IGM cools adiabatically as the universe expands as a^{-2} ,

$$T_{\text{gas}} = 17.9 \text{ K} \left(\frac{T_{\text{CMB},0}}{2.73 \text{ K}} \right) \left(\frac{1+z}{30} \right)^2 \left(\frac{1+z_t}{137} \right)^{-2}. \quad (26)$$

Throughout this epoch, DM halos are continually assembling, but the gas cannot collapse into these halos because of this excess thermal energy and kinetic energy from streaming velocities. The Jeans mass

$$M_J = \frac{\pi^{5/2}}{6} \frac{c_s^3}{(G^3 \rho)^{1/2}} \quad (27)$$

describes the case where gravity overcomes thermal pressure, inducing a collapse, where ρ and $c_s = (\gamma k_B T / \mu m_p)^{1/2}$ are the gas density and sound speed, respectively. Using the IGM temperature T_{gas} and the mean gas density $\bar{\rho}_b = \rho_c \Omega_b (1+z)^3$, one can calculate the cosmological Jeans mass $M_J = 5.85 \times 10^3 [(1+z)/10]^{3/2} M_\odot$ that provides an estimate of the minimum halo mass that can collect baryonic overdensities [36]. The Jeans filtering mass [37],

$$M_F^{2/3}(a) = \frac{3}{a} \int_0^a M_J^{2/3}(a') \left[1 - \left(\frac{a'}{a} \right) \right] da', \quad (28)$$

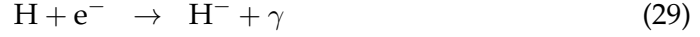
which can be thought as a time-averaged of the Jeans mass, provides a more accurate estimate, and is applicable for any collapsing gas cloud. We will use this quantity in the context of the first stars and galaxies next.

3.2. The first stars

The first generation of stars, known as Population III (Pop III), is inherently different than present-day stars because they form in a neutral, pristine, untouched environ-

ment from a primordial mix of hydrogen and helium. Being metal-free⁵ reduces the cooling ability of the collapsing birth cloud, resulting in stars that are typically more massive than nearby stars [e.g. 38, 39].

Metal-free gas loses its most of its thermal energy through H_2 formation in the gas-phase, using free electrons as a catalyst, in the following reactions.



Recombination leaves behind a residual of free electrons on the order of 10^{-5} . As gas falls into the halos, it shock-heats to around the virial temperature T_{vir} , and its electron fraction is slightly amplified.

But H_2 is a fragile molecule that can be dissociated in the Lyman-Werner (LW) bands between 11.1 and 13.6 eV at soft UV wavelengths through the two-step Solomon process [40], to which energies the universe is optically thin. Furthermore, the intermediary product H^- in the H_2 formation process can be destroyed through the photo-detachment of the extra electron that has an ionization potential of 0.76 eV in the infrared. Accordingly, the timing and host halo masses of Pop III star formation is dependent on the preceding star formation that produces the soft UV and infrared radiation backgrounds. The minimum halo mass that can support sufficient H_2 formation that can induce a catastrophic collapse has been determined as a function of LW background strength as [41],

$$M_{\text{vir}}/M_{\odot} = 1.25 \times 10^5 + 2.86 \times 10^6 J_{21}^{0.47}, \quad (31)$$

where J_{21} is the specific intensity in units of $10^{-21} \text{ erg s}^{-1} \text{ cm}^{-2} \text{ Hz}^{-1} \text{ sr}^{-1}$. Additionally, streaming velocities can suppress Pop III star formation in halos with masses $M \lesssim 10^6 M_{\odot}$ with its exact value depending on the local streaming velocity magnitude that varies on scales of tens of Mpc [e.g. 42].

Simulations of the first stars and galaxies that consider a LW background have found that Pop III stars form at a nearly constant rate of $\sim 3 \times 10^{-5} M_{\odot} \text{ yr}^{-1} \text{ Mpc}^{-3}$ until the end of reionization [e.g. 43]. Each produces a tremendous amount of ionizing radiation because they are thought to be massive with characteristic masses of tens of solar masses [e.g. 44], some forming in binary systems and small clusters [e.g. 45, 46]. They have effective surface temperatures $\sim 10^5 \text{ K}$ that is approximately mass-independent above $20 M_{\odot}$ because of the lack of typical opacities associated with metals in their photospheres. They live for 3–10 Myr and produce between 2×10^{48} and 10^{50} hydrogen ionizing photons per second in the mass range 15–100 M_{\odot} [47]. Most of these photons escape into the nearby IGM, and the averaged escape fraction f_{esc} increases from 20% for a single 15 M_{\odot} star to nearly 90% for a single 200 M_{\odot} star [48]. The exact values of f_{esc} will depend on the total Pop III stellar mass in the halo, the halo mass, and its gas fraction. After their main sequence, a fraction goes supernova, chemically enriching the surrounding few proper kpc, where the exact number depends on their uncertain their initial mass function. Because of this strong feedback, they quench their own formation, blowing out most of the gas that originally existed in their host halos. Furthermore once the medium is enriched with metals, it's 'game over' for Pop III stars in affected regions because by definition, they are metal-free.

⁵ Any element heavier than helium is historically termed a metal in astronomy and astrophysics.

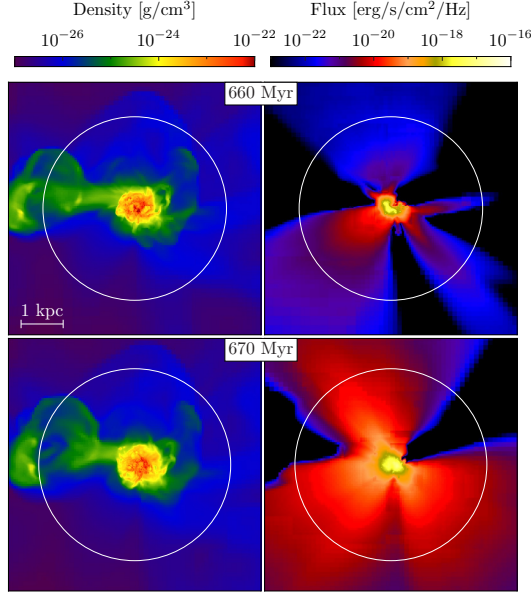


Figure 5. Projections of gas density (left) and UV radiation flux (right) of a first generation galaxy with a stellar mass $\sim 10^5 M_\odot$ at redshift $z \simeq 8$ with the bottom panels pictured 10 Myr after the top panels. The white circle marks the virial radius. The UV escape fractions are 1% (top) and 7% (bottom). Adapted from [52].

3.3. The first galaxies

These heavy elements set the stage for the first galaxies that form in halos above the filtering mass M_F (Equation 28) that depends on the local thermal history of the pre-galactic gas, which was preheated by Pop III radiation and supernovae. Typically, the filtering mass increases from $M_F \sim 3 \times 10^6 M_\odot$ after the first star dies to $M_F \sim 10^8 M_\odot$ about 200 Myr afterwards [43], which is approximately the halo mass in which atomic ($\text{Ly}\alpha$) line cooling is efficient, and accordingly these halos are known as atomic cooling halos ($T \gtrsim 10^4$ K).

The pre-galactic halos are generally gas-poor ($f_{\text{gas}} \equiv M_{\text{gas}}/M_{\text{vir}} \simeq 0.05 - 0.10$) because they are recovering from the gas blowout that their halo progenitors experienced. If the halo is below the atomic cooling limit, star formation is bursty but still intense during active periods, forming between 10^4 and $10^5 M_\odot$ of stars before can cool efficiently through atomic hydrogen transitions. They have star formation rates \dot{M}_\star between 10^{-4} and $10^{-3} M_\odot \text{ yr}^{-1}$, doubling their stellar masses M_\star every ~ 30 Myr (corresponding to a specific star formation rate, $\text{sSFR} \equiv \dot{M}_\star/M_\star \sim 3 \times 10^{-8} \text{ yr}^{-1}$), and producing $\sim 3 \times 10^{49}$ ionizing photons per second. After the halo crosses the atomic cooling limit, it can form stars in a continuous fashion at $\text{sSFR} \sim 3 \times 10^{-8} \text{ yr}^{-1}$, which can vary by an order of magnitude from galaxy to galaxy, depending on how it has been affected by feedback from previous star formation [e.g. 49–51]. By the time the halo mass reaches $10^9 M_\odot$, the first generations of galaxies contain between 10^6 and $10^7 M_\odot$ of metal-poor ($Z \lesssim 0.1 Z_\odot$) stars.

An important quantity in reionization calculations is the uncertain UV escape fraction f_{esc} , which is notoriously difficult to observationally measure and to theoretically calculate. Most reionization models find that $f_{\text{esc}} = 0.1 - 0.2$, independent of halo mass, generally produce reasonable reionization histories [e.g. 53]. In the past decade, there have been great strides in the development of radiation hydrodynamics simulations of the first galaxies in which a direct calculation of f_{esc} is feasible. This

fraction is highly variable from galaxy to galaxy, and even in a single object, it can vary from nearly zero to unity over its formation sequence (see Figure 5). Because the interstellar medium (ISM) is clumpy, the ionization fronts propagate outwards toward to the IGM at varying velocities with respect to angle. The ionizing radiation generally escapes in the directions with small neutral column densities. Once an ionized channel is opened between a star cluster and the IGM, it remains ionized as long as massive stars remain alive. Thus, the value of f_{esc} can be thought as the solid angular fraction that the ionized channels cover. Such efforts have found that the smallest galaxies have high escape fractions. The median time-averaged value of f_{esc} is ~ 0.5 in halos with masses $M_{\text{vir}} \simeq 10^7 M_{\odot}$, and it decreases to 0.05–0.10 at $M_{\text{vir}} \simeq 10^8 M_{\odot}$ [49, 51, 54]. When the total escaping photons are integrated over all galaxies, half of the photon budget to reionization originate from halos with $M_{\text{vir}} \lesssim 10^9 M_{\odot}$.

3.4. The first black holes

Because Pop III stars are thought to be massive, a large fraction will leave a black hole remnant. Depending on their binary fraction, a substantial fraction of Pop III stars may go through a X-ray binary phase, where the secondary star overflows the Roche lobe, which is the Lagrangian point that delineates the gravitational influence of each object, during its giant phase. This material falls toward a stellar-mass black hole remnant of the primary star. In spherical symmetry and neglecting radiation trapping, the accretion rate of black holes is limited by the radiation pressure from the glowing gas around the black hole. When the radiation pressure is equated to the gravitational force, one arrives at the Eddington luminosity,

$$L_{\text{Edd}} = \frac{M_{\text{BH}} c^2}{t_{\text{Edd}}} = \left(\frac{4\pi G m_{\text{p}}}{c \sigma_{\text{T}}} \right) M_{\text{BH}} c^2 = 1.2 \times 10^{38} \left(\frac{M_{\text{BH}}}{M_{\odot}} \right) \text{ erg s}^{-1}, \quad (32)$$

which actually holds for any radiating object. If the efficiency ϵ of converting the rest-mass into radiation is 10%, that is

$$L = \epsilon \dot{M}_{\text{BH}} c^2, \quad (33)$$

the associated mass accretion rate can be calculated by setting $L = L_{\text{Edd}}$, obtaining

$$\dot{M}_{\text{Edd}} = \frac{4\pi G m_{\text{p}} M_{\text{BH}}}{\epsilon c \sigma_{\text{T}}} = 2.22 \times 10^{-8} \left(\frac{\epsilon}{0.1} \right)^{-1} \left(\frac{M_{\text{BH}}}{M_{\odot}} \right) M_{\odot} \text{ yr}^{-1}. \quad (34)$$

It should be noted that the Eddington luminosity and accretion rate can be exceeded when spherical symmetry is broken, occurring when an accretion disk forms around the BH or when radiation is trapped as it scatters within the inflowing gas.

The stellar-mass BH accretes from a multi-color accretion disk that has effective temperatures between 10^4 and 10^7 K with $T \propto R^{-3/4}$ [56], and thus emits strongly in the hard UV and X-ray bands. Their UV luminosities are insignificant when compared to stellar sources, but their X-rays should have an impact on the thermal and ionization state of the IGM. The top panel in Figure 6 shows the evolution of the IGM and how X-rays partially ionize it. Although their number densities depend on the Pop III binary fraction and the active lifetime, results from cosmological simulations have estimated that the IGM is heated to ~ 2000 K and ~ 300 K within 100 kpc and

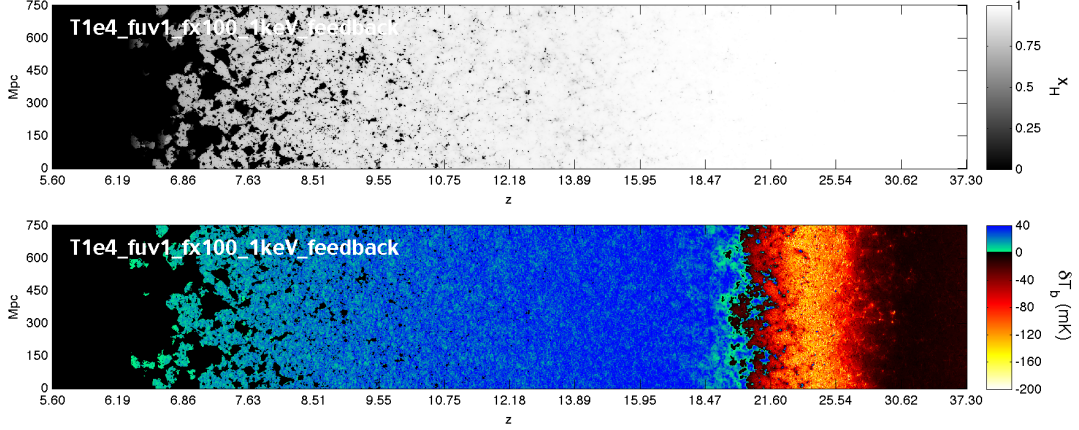


Figure 6. The evolution of the neutral fraction (top panel) and 21 cm brightness temperature (bottom panel) as a function of space and redshift (universe age increases from left-to-right). The blue and red respectively denote emission and absorption in 21 cm. The minimum (yellow-orange) in brightness temperature at $z \sim 25$ in this model occurs when the X-ray heating of the IGM begins. Adapted from [55].

1 Mpc, respectively, of a rare ($3\text{-}\sigma$) galaxy forming region at $z \sim 15$, and it is partially ionized to 1%–2% and 0.1% within 100 kpc and 1 Mpc, respectively [57]. Such IGM pre-heating should be detectable in 21-cm observations [58]. Now that we have covered the basic astrophysics and the theoretical aspects of reionization, we can gain insight on cosmic reionization through some key observations.

4. Constraints from the Edge of the Observable Universe

There are various independent probes of reionization, either measuring the ionization and thermal state of the IGM or the properties of galaxies forming during the EoR. The vast majority of these observations are difficult with the photons streaming across the observable universe to Earth, requiring long exposure times and/or large telescopes. Here we cover the basic physics behind each method and the latest constraints.

4.1. QSO Spectra

As discussed previously, Gunn and Peterson used QSO spectra to determine that the IGM must be highly ionized, otherwise an absorption trough, now termed the Gunn-Peterson (GP) trough, would have been present at $\lambda_\alpha < 1216 \text{ \AA}$. The optical depth to Ly α photons ($n = 1 \rightarrow 2$) is

$$\tau_{\text{GP}} = \frac{\pi e^2}{m_e c^2} f_\alpha \lambda_\alpha H^{-1}(z) n_{\text{HI}}, \quad (35)$$

where m_e is the electron mass, $f_\alpha = 0.4162$ is the upward oscillator strength of the transition, and n_{HI} is the proper neutral hydrogen number density. Evaluated at $z = 6$ with the latest cosmological parameters,

$$\tau_{\text{GP}}(z) = 5.2 \times 10^5 \left(\frac{1+z}{7} \right)^{3/2} \left(\frac{n_{\text{HI}}}{n_{\text{H}}} \right) \quad (36)$$

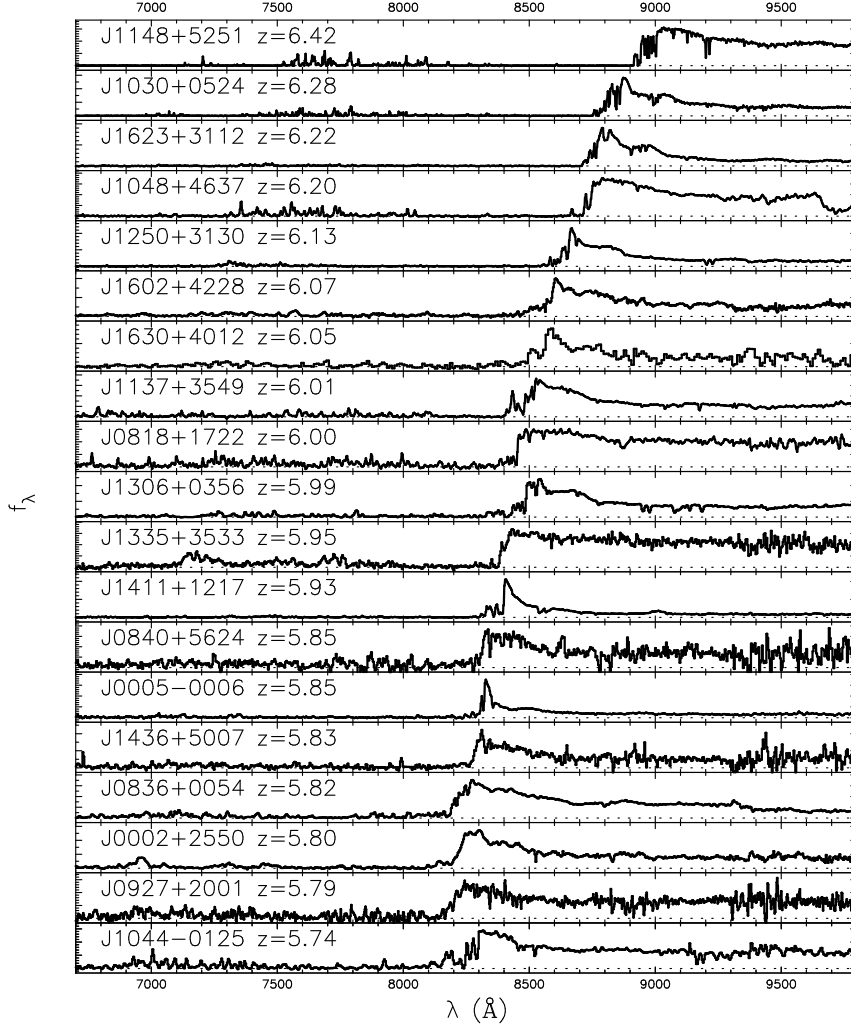


Figure 7. A suite of 19 quasar absorption spectra sorted by descending redshift from top to bottom. The maximum flux in each quasar corresponds to the peak of the Ly α emission line. The light blueward of this peak gradually gets extinguished with increasing redshift until it is completely black (Gunn-Peterson trough) in the top spectra at a redshift $z = 6.42$. Adapted from [59].

showing that the IGM even with a tiny neutral fraction $f_{\text{HI}} \equiv n_{\text{HI}}/n_{\text{H}} \sim 10^{-4}$ will be optically thick to Ly α photons and absorb all light at a wavelength $1216(1 + z_{\text{abs}})$ Å. Because Ly α is such an effective absorber, this method only probes the neutral fraction of highly ionized gas and cannot be used to peer into the EoR.

Figure 7 shows a collection of 19 QSO absorption spectra at $z \simeq 6$ with the GP troughs becoming increasingly opaque with redshift. This is a strong constraint that cosmic reionization is complete by $z \sim 6$. Also, the IGM near the QSO is exposed to a strong radiation field and should be more ionized than the typical IGM. This is known as the proximity effect, resulting in weaker absorption between the Ly α emission line and GP trough. The sizes of these ionized regions are on the order of tens of Mpc at $z \sim 6$ [e.g. 60]. Similar to this type of analysis, absorption from a partially ionized IGM in the proximity zone will produce a damping Ly α wing that occurs when the neutral column density $N_{\text{HI}} \gtrsim 10^{20} \text{ cm}^{-2}$. The spectrum of the current highest redshift QSO at $z = 7.08$ constrains the ionized fraction to be $x_e \simeq 0.60$ at this redshift [61]. On the opposite end, there are still some neutral islands

with sizes up to 160 Mpc at $z = 5.5 - 6$ [62], but they quickly erode as the increasing UV background ionizes them [59], showing that cosmic reionization is indeed an inhomogeneous process.

4.2. Cosmic microwave background

While QSO absorption spectra probe the end of cosmic reionization, the CMB photons travel from the surface of last scattering to Earth and may scatter off free electrons. Thomson scattering polarizes the CMB at large angular scales, resulting in a Thomson scattering optical depth

$$\tau_{\text{es}}(z) = c \sigma_{\text{T}} \int_0^z \frac{\bar{n}_{\text{e}}(z')(1+z')^2}{H(z')} dz' \quad (37)$$

that is directly related to the column density of free electrons. This measure is an integrated one and tells us little about the reionization history and only about the approximate timing of reionization. Here $\sigma_{\text{T}} = 6.65 \times 10^{-25} \text{ cm}^2$ is the Thomson cross-section, $\bar{n}_{\text{e}} = \bar{x}_{\text{e}} \bar{n}_{\text{H}}(1 + \eta Y/4X)$ is the mean comoving electron number density, $\bar{x}_{\text{e}}(z)$ is the mean ionized fraction, and \bar{n}_{H} is the mean comoving hydrogen number density. We assume that helium is singly ionized ($\eta = 1$) at $z > 3$ in the same volume fraction as hydrogen and doubly-ionized ($\eta = 2$) at later times. $X = 0.76$ and $Y = 1 - X$ are the hydrogen and helium number fractions, respectively.

A fully ionized IGM between $z = 0$ and $z = 6$ results in $\tau_{\text{es}} = 0.039$, and the remaining portion ($z > 6$) of the integral depends on the reionization history $x(z)$. The most recent Planck 2016 [63] measurement of $\tau_{\text{es}} = 0.058 \pm 0.012$, corresponding to a reionization redshift $z_{\text{re}} = 8.8 \pm 0.9$ when $x_{\text{e}} = 0.5$. It should be noted that the Thomson optical depth has been curiously decreasing with every new measurement, starting with the *WMAP* mission and continuing with the *Planck* mission [see Figure 41 in 64].

In addition to the Thomson optical depth, the scattering of CMB photons introduces temperature anisotropies through the Doppler effect if there are variations in the baryon density ρ_{b} or ionization fraction x_{e} , known as the kinetic Sunyaev-Zel'dovich (kSZ) effect [65]. The differential contribution to the temperature anisotropy in the line-of-sight $\hat{\mathbf{n}}$ between a redshift interval $z \rightarrow z + dz$ is

$$\frac{dT_{\text{kSZ}}}{T_{\text{CMB}}}(\hat{\mathbf{n}}) dz = \sigma_{\text{T}} \frac{\bar{n}_{\text{e}}(z)(1+z)^2}{H(z)} \exp[-\tau_{\text{es}}(z)](\hat{\mathbf{n}} \cdot \mathbf{q}) dz, \quad (38)$$

where $\mathbf{q}(\mathbf{r}) = [x_{\text{e}}(\mathbf{r})/\bar{x}_{\text{e}}][\rho_{\text{b}}(\mathbf{r})/\bar{\rho}_{\text{b}}]\mathbf{v}(\mathbf{r})$ accounts for ionization and density fluctuations at some position \mathbf{r} , and \mathbf{v} is the bulk motion of free electrons with respect to the CMB. Notice how this expression is similar to the Thomson optical depth (Equation 37) but modified by the optical depth and the line-of-sight anisotropies \mathbf{q} . The kSZ effect during inhomogeneous reionization produces excess power at multipole moments $\ell \simeq 3000$, corresponding to an angle $\theta \simeq 3.6'$ and comoving scale $L \simeq 14.6 \text{ Mpc}$. The amount of power depends on the timing and duration of reionization, where more extended reionization histories result in larger fluctuations at this ℓ for a fixed τ_{es} [e.g. 66–69]. The South Pole Telescope has measured the CMB power spectrum at these high- ℓ [70]. By comparing these data to reionization simulations, they constrained its duration, defined to be the time elapsed between

$x_e = 0.2 \rightarrow 0.99$, to be $\Delta z_{\text{re}} < (4.4, 7.9)$ in their optimistic and conservative models, respectively.

4.3. The Ly α forest

The Ly α forest denotes the myriad of Ly α narrow absorption lines coming from clouds in the IGM. They become more abundant with increasing redshift [71] and probe clouds with column densities $\log(N_{\text{HI}}/\text{cm}^{-2}) = 12 - 16$. These lines become so abundant that they start to block out all of the background light, transforming into a GP trough at $z \sim 6$. One constraint on the ionized fraction is the ‘dark fraction’ of QSO spectra in the Ly α forest that originate from either neutral patches or residual neutral hydrogen in ionized regions [72]. Taken at $z = 5.9$, the dark fraction in the Ly α forest results in an lower limit of $x_e > 0.94$ [73].

Because Ly α forest clouds contain such small column densities, they are prone to ionization and heating from the ultraviolet background (UVB) produced by galaxies and quasars, and thus are excellent thermometers of the post-reionization universe. The UVB can be quantified by the hydrogen ionization rate

$$\Gamma(z) = 4\pi \int_{\nu_{912}}^{\infty} J_{\nu}(z) \sigma_{\text{HI}}(\nu) \frac{d\nu}{h\nu}, \quad (39)$$

where σ_{HI} is the photoionization cross-section, J_{ν} is the specific intensity, and $\nu_{912} = 3.28 \times 10^{15}$ Hz is the frequency of the Lyman limit. The ionization rate can be derived from the Ly α forest lines, provided its temperature and optical depth to Ly α photons. The temperature can be calculated from Ly α forest line widths, which are affected by the Doppler effect of thermal motions of neutral hydrogen in the clouds and the thermal smoothing of the absorber over the time it has been exposed to the UVB. The optical depth can be calculated in photoionization equilibrium [74]. Data from the Sloan Digital Sky Survey [SDSS; 75] has shown that the ionization rate is relatively constant between $z = 2 - 5$ and sharply increasing with time between $z = 5 - 6$ [76]. The ratio of ionizing to non-ionizing radiation increases by a factor of ~ 3 going from $z = 3$ to $z = 5$, suggesting that galaxies are more efficient producers of ionizing photons at earlier times. Lastly, the sharp evolution in Γ at $z > 5$ could be caused by either an increase in ionizing emissivity from galaxies and black holes or the opacity of the IGM. The latter decreases after EoR as dense neutral clouds are photo-evaporated by the UVB, increasing the mean-free path of ionizing photons.

The thermal history of the IGM, probed by the Ly α forest, is an indirect measure of the reionization history and places constraints on the ionizing source spectra. After the cloud has been heated by some radiation source, it never reaches thermal equilibrium, and it is heated by the UVB and cools adiabatically [77],

$$\frac{dT}{dt} = \frac{2}{3k_{\text{B}}} E \alpha_{\text{B}}(T) n_{\text{e}} - 2TH(z), \quad (40)$$

where E is the average photoheating energy (photon energy minus the ionization potential of hydrogen, 13.6 eV), and α_{B} is the case B recombination rate coefficient (Equation 12). Several groups have found that the typical IGM temperature is $\sim 10^4$ K at $z = 5$ [e.g. 76, 78]. Equation (40) implies that the low-density IGM has a long cooling timescale and thus has a thermal memory of reionization. The exact thermal evolution depends on the timing of the initial photoheating, giving the time

available to cool to $\sim 10^4$ K at $z = 5$ and the spectral hardness of ionizing sources [79, 80]. At later times, the double ionization of helium increases the mean IGM temperature to 3×10^4 K at $z = 2$ [e.g. 81].

4.4. Neutral hydrogen (21 cm) emission

Perhaps the most direct measure of cosmic reionization comes from neutral hydrogen emission of the hyperfine splitting of the ground state, the 21 cm ($\nu = 1420.4$ MHz; $E_{21} = 5.87 \times 10^{-6}$ eV) transition. The hydrogen atom has a slightly lower energy when the spins of its proton and electron are anti-parallel than when they are parallel. The first detection of extraterrestrial 21-cm emission from neutral hydrogen happened in 1951 [82, 83], and it was not until four decades later that it was realized that 21-cm observations could be used to probe reionization [84].

When the IGM is mostly neutral, the universe is glowing in this radiation and most of it is not absorbed as it travels toward Earth. Its detection is complicated by astrophysical foreground and terrestrial sources, especially considering that the redshifted 21-cm emission is at $142[(1+z)/10]^{-1}$ MHz. Before any stars form, the spin temperature

$$T_s = T_* \ln \left(\frac{3n_0}{n_1} \right) \quad (41)$$

measures the relative occupancy of the electron spin levels. Here $T_* = E_{21}/k_B = 0.0682$ K, and n_0 and n_1 are the singlet and triplet hyperfine levels of the ground state. The factor of 3 comes from the ratio of statistical weights between these levels. The spin temperature tightly couples to the CMB temperature $T_{\text{CMB}} = 2.73(1+z)$ K because the gas density is not high enough to couple with the kinetic temperature T_K that cools as a^{-2} from adiabatic cosmic expansion (Equation 26).

After the first stars form, their Ly α emission couples the spin and kinetic temperatures of neutral hydrogen together through the Wouthuysen-Field (WF) effect [85, 86], in which a Ly α photon promotes a ground state electron to the $n = 2$ excited state that spontaneously decays back into the ground state that can have a different spin state than the original one. Considering the CMB temperature, atomic collisions, and the WF effect, the spin temperature is a weighted mean of the three processes

$$T_s^{-1} = \frac{T_{\text{CMB}}^{-1} + x_c T_K^{-1} + x_\alpha T_c^{-1}}{1 + x_c + x_\alpha}, \quad (42)$$

where x_c and x_α are the collisional and Ly α coupling coefficients [87]. The latter coefficient rapidly increases from 10^{-3} to 100 in the redshift range $z = 30 - 10$, reaching unity at $z \sim 20$ and is sensitive to the nature of the ionizing sources. T_c is the color temperature that is determined by the spin-flip transition rates in the WF effect. Because the IGM is highly opaque to Ly α photons, a thermal equilibrium is reached between the Ly α photons and kinetic motions of the atoms, resulting in $T_c \approx T_K$. The spin temperature thus simplifies to

$$T_s^{-1} = \frac{T_{\text{CMB}}^{-1} + (x_c + x_\alpha) T_K^{-1}}{1 + x_c + x_\alpha}. \quad (43)$$

Absorption or emission by neutral hydrogen changes the 21 cm (differential) brightness temperature T_b , which is the temperature relative to the background (CMB) temperature. Using the current cosmological parameters, it is given by

$$T_b \simeq 26.9 \left(\frac{1+z}{10} \right)^{1/2} \left(\frac{T_s - T_{\text{CMB}}}{T_s} \right) \text{ mK}, \quad (44)$$

where Equation (43) can be rearranged as

$$\frac{T_s - T_{\text{CMB}}}{T_s} = \frac{x_c + x_\alpha}{1 + x_c + x_\alpha} \left(1 - \frac{T_{\text{CMB}}}{T_K} \right). \quad (45)$$

In addition to the neutral fraction, Figure 6 also shows the evolution of the spatial distribution of T_b from a numerical reionization model [55]. Positive and negative values denote emission and absorption at 21 cm. $\text{Ly}\alpha$ coupling becomes dominate after $z \sim 30$ as the first stars begin to form, driving a decrease in T_b . Then the IGM begins to be partially ionized and heated by X-ray sources, whose radiation has very large mean free paths ($\lambda_{\text{mfp}} \propto E^{-3}$). Two candidate X-ray source types are X-ray binaries, composed of a stellar-mass black hole and a massive star, or relatively light black holes at the centers of the first galaxies that are the progenitors of the present-day SMBHs. This heating increases T_K and thus T_b . Eventually the IGM becomes ionized by UV sources and $T_K \gg T_{\text{CMB}}$, causing the emission T_b to asymptote to a value independent of the spin temperature, i.e. both sides of Equation (45) approach unity.

A measurement of the brightness temperature evolution would place strong constraints on the reionization history and the nature of the ionizing sources. In particular, the location of the trough in T_b will relay information about the $\text{Ly}\alpha$ and X-ray emissivities of the first stars, black holes, and galaxies. There are several experiments aiming for such a measurement, which include PAPER [88], LOFAR [89], MWA [90], HERA [91], and SKA [92].

4.5. Sources of reionization

From the direct and indirect IGM observations just discussed, cosmic reionization occurred between $z = 6 - 15$, but what sources were responsible for producing the required ionizing radiation for such a phase transition? QSOs are some of the brightest objects in the universe, but their number densities are not high enough [e.g. 93] to significantly contribute to the UVB and the overall photon budget of reionization. The latest studies have shown that they only contribute 1–5% of the photon budget at $z = 6$ [e.g. 94, 95], however see Madau & Haardt [96] for a counterpoint. This leaves starlight from galaxies to propel reionization. Two important characteristics of high-redshift galaxies during the EoR are: *How abundance are galaxies as a function of luminosity and redshift?* *How many ionizing photons escaped from these galaxies into the IGM?* The first question is addressed by counting galaxies and computing a luminosity function (LF), and the second is a harder quantity to measure as a neutral IGM is opaque to ionizing photons and needs to be inferred from their UV continuum redward of $\text{Ly}\alpha$.

Recent observational campaigns have provided valuable constraints on the nature of the first galaxies, their central BHs, and their role during reionization. In the rest-

frame UV, the Hubble Space Telescope (HST) *Ultra Deep Field* [97] and *Frontier Fields* campaigns [98] can probe galaxies with stellar masses as small as $10^7 M_\odot$ at $z \gtrsim 6$ and as distant as $z \simeq 11$ [99, 100]. The LF is best described with a Schechter fit [101] as a function of luminosity,

$$\phi(L) = \phi^* \left(\frac{L}{L^*} \right)^\alpha \exp \left(-\frac{L}{L^*} \right) \quad (46)$$

or absolute magnitude M

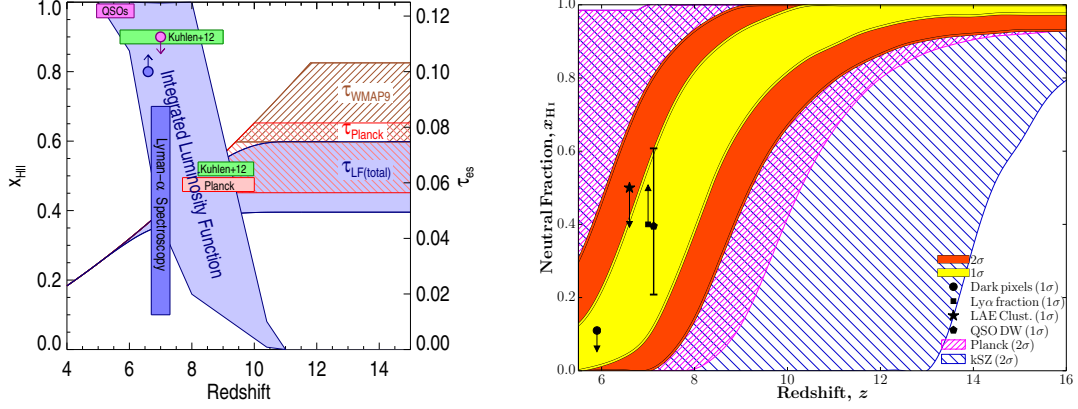
$$\phi(M) = \frac{\ln(10)}{2.5} \phi^* 10^{0.4(M-M^*)(\alpha+1)} \exp \left[-10^{-0.4(M-M^*)} \right] \quad (47)$$

that exponentially decays at the bright-end and is a power law at the faint-end. There are three parameters in this fit: the characteristic luminosity L^* (or magnitude M^*) that denotes the transition between power-law and exponential decay, the number density normalization ϕ^* , and faint-end slope α . For the purposes of reionization sources, the faint-end is the most relevant because these faint galaxies should be very numerous. The faint-end slope and the luminosity at which the LF flattens is key when computing the total number density of galaxies and their ionizing emissivity. Various groups have constrained $\alpha \simeq -2$ at $z \geq 6$ [e.g. 102], and there are slight hints from the *Frontier Fields* that the LF flattens above a UV absolute magnitude of -14 [103, 104]. Based on this steep slope, there should be an unseen population of even fainter and more abundant galaxies that will eventually be detected by next-generation telescopes, such as JWST (James Webb Space Telescope) and 30-m class ground-based telescopes.

The ionizing emissivity (ρ_{UV} ; in units of $\text{erg s}^{-1} \text{Hz}^{-1} \text{Mpc}^{-3}$) is a key quantity in reionization calculations. The observed LF can be integrated down to some limiting magnitude, below which galaxies are suppressed due to feedback effects, to obtain a star formation rate density (in units of $M_\odot \text{yr}^{-1} \text{Mpc}^{-3}$). This quantity can then be converted into the ionizing emissivity with two factors. The first is the number of ionizing photons emitted per stellar baryon $f_\gamma \simeq 4000 - 13000$, which depends on stellar metallicity. The second and most uncertain is the fraction f_{esc} of ionizing photons that escape into IGM. Finkelstein et al. [105] used $\text{Ly}\alpha$ forest observations to place an upper limit on the average $\langle f_{\text{esc}} \rangle < 0.13$ at $z = 6$. However this does not prevent the average escape fraction from being larger at higher redshifts [53]. Direct measurements of f_{esc} is impossible during EoR because the IGM optical depth in the $\text{Ly}\alpha$ forest only drops to unity at $z \sim 3$ as these absorption systems become less abundant with time. Nevertheless, deep narrow-band galaxy spectroscopy and imaging have detected Lyman continuum emission in numerous $z \sim 3$ galaxies with f_{esc} values ranging from an upper limit of 7%–9% for bright galaxies [106] to 10%–30% for fainter $\text{Ly}\alpha$ emitters [107] and $33 \pm 7\%$ for ‘Lyman-continuum galaxies’ [108]. These measurements combined with theoretical calculations may be taken as a guide to the f_{esc} values expected from EoR galaxies.

Two additional, albeit weaker, constraints come from $\text{Ly}\alpha$ emitters, defined as galaxies with $\text{Ly}\alpha$ emission lines with equivalent widths⁶ $> 25 \text{ \AA}$. At $z \sim 6$, nearly 50% of faint galaxies ($M_{\text{UV}} > -20.25$) are $\text{Ly}\alpha$ emitters [109], but this steeply decreases to 20%–30% at $z \sim 7$ [e.g. 110] in accordance with the IGM becoming more

⁶An integrated measure of the emission or absorption line, normalized by the adjacent continuum, that is defined as $\int (f_\lambda / f_{\text{cont}}) d\lambda$, and its integration limits span the entire line.



(a) Constraints on the ionized fraction from QSO spectra, galaxy LFs, Ly α forest and GP troughs, a reionization model [115], and the Planck and WMAP measurements of τ_{es} . Adapted from [116].

(b) Constraints on the neutral fraction, using a Markov chain Monte Carlo method with semi-numeric reionization calculations (see Section 5.2), with several independent priors. Adapted from [73].

Figure 8. Compilations of observational constraints on the history of cosmic reionization.

neutral and having a larger optical depth to Ly α photons, absorbing the emergent Ly α emission line [111]. This change in Ly α fraction has been used in models that predict an increase in x_e by at least 40% from $z = 7$ to $z = 6$ [112]. The second Ly α emitter constraint comes from their clustering [e.g. 113, 114], in that galaxies living closer to neutral patches will experience more Ly α extinction. This signal is determined by the typical host DM halo mass and the electron fraction. This method provides a single constraint of $x_e \geq 0.5$ at $z = 6.6$ [73].

4.6. Summary of observations

Having reviewed the primary observational constraints on cosmic reionization, there are clearly several independent measures of this grand event. All of these constraints are summarized in Figure 8 from Finkelstein et al. [116] and Greig et al. [73]. The end of reionization is probed by QSO absorption spectra in which the Ly α forest, and at $z \gtrsim 6$ the GP trough, is used to constrain the residual neutral fraction ($\simeq 10^{-4}$ at $z = 6$) and remaining neutral patches that can span up to 160 Mpc. The thermal state of the Ly α forest retains some ‘fossil memory’ of its initial heating during reionization and can be used to constrain the timing and heating source spectrum. Furthermore, the evolution of the UVB is measured from the Ly α forest and is steeply increasing with time at $z > 5$. The CMB provides both an integral measure of reionization with the universe being half-ionized at $z_{\text{re}} = 8.8 \pm 0.9$ and constraints of its duration ($\Delta z_{\text{re}} < 7.9$) through the kSZ effect. Future 21 cm experiments will be able to further constrain the reionization history and the nature of the ionizing sources. Galaxies are most likely the primary driver of reionization from the measurement of the steep faint-end slope $\alpha \simeq -2$ of the galaxy LF at $z \geq 6$ that results in an increasing ionizing emissivity as galaxies assemble during the first billion years after the Big Bang.

5. Reionization Modeling

Cosmic reionization can be modeled in a variety of methods, ranging from a volume-averaged approach, taking less than a second to compute, to full radiation hydrodynamics cosmological simulations of galaxies and the IGM, taking months to complete. These methods have their advantages and disadvantages, and they complement each other. They use the appropriate observational constraints to make predictions about the reionization history, the nature of its sources, and promising future observational techniques and measures on further constraining this epoch.

5.1. Volume-averaged analytical models

On the most basic level, reionization models count the number of ionizing photons and compare it with the number of hydrogen atoms in some specified volume, which was first, to be best of our knowledge, studied by Arons & McCray [117] in a time-dependent approach. As we have covered in the basic physics of ionization balance, recombinations can still occur in a strong ionizing radiation field, and thus cosmic reionization requires more than one ionizing photon per hydrogen atom. The rate of change in the ionized fraction x_e of the universe can be computed by considering the comoving photon emissivity \dot{n}_γ and recombinations in the ionized regions,

$$\frac{dx_e}{dt} = \frac{\dot{n}_\gamma}{\bar{n}_H} - \frac{x_e}{\bar{t}_{\text{rec}}}, \quad (48)$$

This differential equation is integrated from a neutral medium ($x_e = 0$) at very early times before any UV sources form ($z \sim 50 - 100$) until the universe is completely ionized ($x_e = 1$). Its evolution gives a reionization history, which then can be integrated to obtain the optical depth to Thomson scattering (Equation 37).

Here \bar{n}_H is the mean comoving hydrogen number density, and $\bar{t}_{\text{rec}} = [C\alpha_B n_{H,0}(1 + Y/4X)(1 + z)^3]^{-1}$ is an effective recombination time. Recall that $X = 0.76$ and $Y = 1 - X$ are the hydrogen and helium number fractions, respectively. The clumping factor $C \approx 3 - 5$ during EoR accounts for enhanced recombinations in an ionized clumpy IGM [e.g. 118, 119]. There are various definitions for the clumping factor [see 120, for a discussion], but the most straightforward definition is $C \equiv \langle \rho^2 \rangle / \langle \rho \rangle^2$ and is restricted to ionized regions.

To calculate the number density of ionizing photons \dot{n}_γ that escape into the IGM, we first must calculate the fraction of matter that has collapsed into DM halos and then luminous objects. Most of the uncertainties in reionization modeling originates from the halo-galaxy connection. More specifically, given a DM halo, the following main ingredients are needed to calculate the ionizing emissivity: (i) the star formation rate or stellar mass, (ii) the stellar ionizing efficiency (i.e. number of ionizing photons per stellar baryon), and (iii) the UV escape fraction. For a time and halo mass independent model [e.g. 121, 122], $\dot{n}_\gamma = f_{\text{esc}} f_\gamma \bar{\rho}_\star$, where $\bar{\rho}_\star$ is the star formation rate density and recall that f_γ is the photon to stellar baryon ratio. However, simulations have shown that star formation rates and f_{esc} values are strong functions of halo mass M . A more accurate value for the ionizing emissivity can be calculated by integrating over all halo masses,

$$\dot{n}_\gamma = \int_{M_{\text{min}}}^{\infty} f_{\text{esc}} f_\gamma (f_{\text{gas}} f_\star \dot{f}_c M_{\text{vir}}) dM_{\text{vir}}, \quad (49)$$

where *all* of the factors are functions of halo mass, and the product inside the parentheses is the star formation rate density in halo masses between M and $M + dM$. Here M_{\min} is the minimum halo mass that hosts star formation; $f_{\text{gas}} \equiv M_{\text{gas}}/M_{\text{vir}}$ is the gas fraction in a halo; $f_{\star} \equiv M_{\star}/M_{\text{gas}}$ is the star formation efficiency from this gas, and \dot{f}_c is the time derivative of the collapsed mass fraction in halos (Equation 8). This integral can be solved numerically if given functional forms (either smooth or piecewise [e.g. 52, 123]) of these factors, which are usually computed from simulations [e.g. 124] or semi-analytic models [e.g. 125] of early galaxy formation.

5.2. Semi-numeric models

The latest observational constraints strongly suggest that reionization is driven by galaxies and their UV radiation, and thus it is a relatively local process. Semi-numeric models originated from an analytical (excursion set) treatment of reionization [126] that made the fundamental assumption that overdense regions drive reionization. With this assumption, one asserts that if the number of ionizing photons, corrected for recombinations, exceeds the number of baryons in some region, then the region must be ionized. This model has been extended to three-dimensional volumes [e.g. 123, 127, 128] and can accurately generate full density, velocity, and ionization fields without the need to follow the underlying physics.

From a single set of cosmological initial conditions, usually given in a 3-D lattice with N_{cell}^3 computational cells, at high redshift $z \sim 100$, semi-numeric models can compute the ionized fraction for each cell. One major advantage to this method is that these models can calculate $x_e(\mathbf{r})$ at any redshift without performing a time-dependent integral. Namely, a cell is considered to be ionized when

$$f_c(r, M_{\min}, R, z) \geq \zeta^{-1}, \quad (50)$$

where ζ is the ionization efficiency, and f_c is the collapsed mass fraction (Equation 8) inside a sphere of radius R in halos with masses $M > M_{\min}$. This value of R is iterated from a large length, usually the UV photon mean free path, down to the width of a single cell. The ionization efficiency can be parameterized [e.g. 73], not unlike analytical models, as

$$\zeta = 30 \left(\frac{f_{\text{esc}}}{0.2} \right) \left(\frac{f_{\star}}{0.03} \right) \left(\frac{f_b}{\Omega_b/\Omega_m} \right) \left(\frac{f_{\gamma}}{4000} \right) \left(\frac{1.5}{1 + n_{\text{rec}}} \right), \quad (51)$$

where n_{rec} is the average number of recombinations per IGM baryon. These three parameters fully determine the ionization state at any time and position. The most computationally intensive portion of semi-numeric calculations involves Fast Fourier Transforms (FFTs) and usually takes on the order of core-hours for a single 2048^3 realization, including initial condition generation.

5.3. Cosmological radiative transfer simulations

Cosmological N -body DM-only simulations compute the cosmic density field and halo catalog, which is then used to calculate the evolution of time- and space-dependent ionization fields. They assume that gas follows the DM, which is a good assumption on large-scales and in larger halos ($M \gtrsim 10^9 M_{\odot}$), and then populate these

halos with galaxies that produce ionizing radiation. Given a density field at some redshift z and the associated halos, the radiation is transported through the IGM, usually with ray tracing solving the cosmological radiative transfer equation, which in comoving coordinates [129] is

$$\frac{1}{c} \frac{\partial I_\nu}{\partial t} + \frac{\hat{\mathbf{n}} \cdot \nabla I_\nu}{\bar{a}} - \frac{H}{c} \left(\nu \frac{\partial I_\nu}{\partial \nu} - 3I_\nu \right) = -\kappa_\nu I_\nu + j_\nu, \quad (52)$$

reproducing inhomogeneous reionization. Here $I_\nu \equiv I(\nu, \mathbf{x}, \Omega, t)$ is the radiation specific intensity in units of energy per time t per solid angle per unit area per frequency ν . $H = \dot{a}/a$ is the Hubble parameter. $\bar{a} = a/a_{em}$ is the ratio of scale factors at the current time and time of emission. The second term represents the propagation of radiation, where the factor $1/\bar{a}$ accounts for cosmic expansion. The third term describes both the cosmological redshift and dilution of radiation. On the right hand side, the first term considers the absorption coefficient $\kappa_\nu \equiv \kappa_\nu(\mathbf{x}, \nu, t)$, and the second term $j_\nu \equiv j_\nu(\mathbf{x}, \nu, t)$ is the emission coefficient that includes any point sources of radiation or diffuse radiation.

Solving this equation is difficult because of its high dimensionality; however, we can make some appropriate approximations to reduce its complexity in order to include radiation transport in numerical calculations. Typically timesteps in dynamic calculations are small enough so that $\Delta a/a \ll 1$, therefore $\bar{a} = 1$ in any given timestep, reducing the second term to $\hat{\mathbf{n}} \partial I_\nu / \partial \mathbf{x}$. To determine the importance of the third term, we evaluate the ratio of the third term to the second term. This is HL/c , where L is the simulation box length. If this ratio is $\ll 1$, we can ignore the third term. For example at $z = 5$, this ratio is 0.1 when $L = c/H(z = 5) = 53$ proper Mpc. In large boxes where the light crossing time is comparable to the Hubble time, then it becomes important to consider cosmological redshifting and dilution of the radiation. Thus equation (52) reduces to the non-cosmological form in this local approximation,

$$\frac{1}{c} \frac{\partial I_\nu}{\partial t} + \hat{\mathbf{n}} \frac{\partial I_\nu}{\partial \mathbf{x}} = -\kappa_\nu I_\nu + j_\nu. \quad (53)$$

Ray tracing methods represent the source term j_ν as point sources of radiation (e.g. stars, quasars) that emit radial rays that are propagated along the direction $\hat{\mathbf{n}}$.

The downside to this method is that it neglects any hydrodynamics and must make assumptions about the ionizing luminosity escaping from the halos, the IGM clumping factor C , and the suppression of star formation in low-mass ($M \lesssim 10^9 M_\odot$) halos. Such calculations are performed in either (i) post-processing with the radiative transfer calculated on density field and halo catalog written to disk, or (ii) inline where the halo catalogs and radiation sources are computed on-the-fly, and radiation is traced through the density field that is stored in memory. The largest simulations to-date have over 100 billion particles and simulate domains of over 500 comoving Mpc on a side, and such simulations consume a couple of million core-hours [e.g. 130]. They produce similar results as semi-numeric models but with a larger dynamic range, with higher resolution in collapsed regions, thus can follow the small-scale ionization fluctuations to greater accuracy.

5.4. Full radiation hydrodynamics simulations

Perhaps the most accurate and computationally expensive calculations are full radiation hydrodynamics simulations of cosmological galaxy formation and reionization. Only in the past decade or so, computational resources have become large enough, along with algorithmic advances, to cope with the requirements of such calculations. There are two popular methods to solve the radiative transfer equation coupled to hydrodynamics in three dimensions:

- *Moment methods*: The angular moments of the radiation field describe its angular structure, which are related to energy, flux, and radiation pressure [131]. These have been implemented in conjunction with short characteristics [132], with long characteristics [133], with a variable Eddington tensor in the optically-thin limit [134] and the general case [135], and with an M1 closure relation [136, 137]. Moment methods have the advantage of being efficient and independent of the number of radiation sources. However, they are diffusive and result in incorrect shadows in some situations.
- *Ray tracing*: Radiation can be propagated along rays that extend through a computational grid [e.g. 138–140] or particle set [e.g. 141–143], as discussed previously. In general, these methods are very accurate but computationally expensive because the radiation field must be well sampled by the rays with respect to the spatial resolution of the domain.

In addition to following the DM dynamics, like in the radiative transfer simulations, they follow the hydrodynamics of the cosmological domain that allows for the treatment of gaseous collapses within halos that are driven by radiative cooling. These radiative processes are computed through a non-equilibrium chemical network [e.g. 144]. However computational run-time and memory limits the resolution of these simulations, which are typically ~ 10 times more expensive than the cosmological radiative transfer simulations. Depending on the domain size and resolution, ‘sub-grid’ star formation prescriptions spawn particles that represent either entire galaxies or individual stellar clusters. Based on this prescription, the particle has an ionizing luminosity, whose radiation is the source of the radiative transfer equation (Equation 52 or 53). Because the radiation transport is coupled with the hydrodynamics, this equation must be solved with either small timesteps and/or the appropriate approximations [140]. Thus, the radiation sources and the ensuing hydrodynamic response can be modeled without relying on a halo-galaxy relationship. The suppression of star formation, especially in low-mass galaxies can be directly modeled, along with the regulation of star formation that results in a more accurate description of the ionizing sources during the EoR and the process of reionization itself. That being said, there still exists uncertainties, arising from the sub-grid models and convergence issues of the numerical solvers with respect to resolution.

6. Conclusions

Cosmic reionization is the last cosmological phase transition. There is strong observational evidence that it ended nearly one billion years after the Big Bang. The first generations of galaxies primarily powered this grand event in the cosmic timeline. Because structure forms hierarchically, these first galaxies are the building blocks of all galaxies we see today, and their properties are passed along as galaxies assem-

ble. Thus, further constraints from the epoch of reionization will play a key role in solidifying theories of galaxy formation and cosmology.

However there still are unanswered questions in its exact timing, its progression, its nature, and the role of the first galaxies played during the epoch of reionization. These questions will be elucidated with the upcoming James Webb Space Telescope, ground-based 30-m class telescopes, and more accurate CMB and 21-cm experiments, all set to be commissioned within the next decade. Observing both the reionizing universe and the galaxies responsible for this transition is paramount in augmenting our knowledge of this formative period in the universe.

Acknowledgments

Many throughout my academic career have contributed to my understanding of the first stars, first galaxies, radiation transport, and reionization, but I want to give special thanks to Tom Abel, Marcelo Alvarez, Renyue Cen, Andrea Ferrara, Andrei Mesinger, Michael Norman, Brian O’Shea, Britton Smith, and Matthew Turk. My research is currently supported by National Science Foundation (NSF) grants AST-1333360 and AST-1614333 and Hubble theory grants HST-AR-13895 and HST-AR-14326.

Notes on contributor



John Wise is the Dunn Family Associate Professor in the School of Physics and Center for Relativistic Astrophysics at the Georgia Institute of Technology. He received his B.S. in Physics from the Georgia Tech in 2001. He then studied at Stanford University, where he received his Ph.D. in Physics in 2007. He went on to work at NASA’s Goddard Space Flight Center as a NASA Postdoctoral Fellow. Then in 2009, he was awarded the Hubble Fellowship which he took to Princeton University before arriving at Georgia Tech in 2011, coming back home after ten years roaming the nation. He uses numerical simulations to study the formation and evolution of galaxies and their black holes. He is one of the lead developers of the community-driven, open-source astrophysics code Enzo (enzo-project.org) and has vast experience running state-of-the-art simulations on the world’s largest supercomputers.

References

- [1] Minkowski R. A New Distant Cluster of Galaxies. *ApJ*. 1960 Nov;132:908–910.
- [2] Matthews TA, Bolton JG, Greenstein JL, et al. paper presented at the 107th meeting of the AAS. In: American Astronomical Society Meeting Abstracts; Vol. 107; Dec.; 1960.
- [3] Schmidt M. 3C 273 : A Star-Like Object with Large Red-Shift. *Nature*. 1963 Mar; 197:1040.
- [4] Hoyle F, Fowler WA. On the nature of strong radio sources. *MNRAS*. 1963;125:169.
- [5] Schmidt M, Matthews TA. Redshift of the Quasi-Stellar Radio Sources 3c 47 and 3c 147. *ApJ*. 1964 Feb;139:781.
- [6] Sandage A. The Existence of a Major New Constituent of the Universe: the Quasistellar Galaxies. *ApJ*. 1965 May;141:1560.

- [7] Osterbrock DE, Parker RAR. Excitation of the Optical Emission Lines in Quasi-Stellar Radio Sources. *ApJ*. 1966 Jan;143:268.
- [8] Salpeter EE. Accretion of Interstellar Matter by Massive Objects. *ApJ*. 1964 Aug; 140:796–800.
- [9] Zel'dovich YB. The Fate of a Star and the Evolution of Gravitational Energy Upon Accretion. *Soviet Physics Doklady*. 1964 Sep;9:195.
- [10] Lynden-Bell D. Galactic Nuclei as Collapsed Old Quasars. *Nature*. 1969 Aug;223:690–694.
- [11] Tananbaum H, Avni Y, Branduardi G, et al. X-ray studies of quasars with the Einstein Observatory. *ApJ*. 1979 Nov;234:L9–L13.
- [12] Gunn JE, Peterson BA. On the Density of Neutral Hydrogen in Intergalactic Space. *ApJ*. 1965 Nov;142:1633–1641.
- [13] Planck Collaboration, Ade PAR, Aghanim N, et al. Planck 2015 results. XIII. Cosmological parameters. *A&A*. 2016 Sep;594:A13.
- [14] Rees MJ. The Universe at $z > 5$: When and How Did the 'Dark Age' End? In: N R Tanvir, A Aragon-Salamanca, & J V Wall, editor. *The Hubble Space Telescope and the High Redshift Universe*; 1997. p. 115–+.
- [15] Skillman SW, Warren MS, Turk MJ, et al. Dark Sky Simulations: Early Data Release. *ArXiv e-prints* (14072600). 2014 Jul;.
- [16] Peebles PJE. Large-scale background temperature and mass fluctuations due to scale-invariant primeval perturbations. *ApJ*. 1982 Dec;263:L1–L5.
- [17] Blumenthal GR, Faber SM, Primack JR, et al. Formation of galaxies and large-scale structure with cold dark matter. *Nature*. 1984 Oct;311:517–525.
- [18] Davis M, Efstathiou G, Frenk CS, et al. The evolution of large-scale structure in a universe dominated by cold dark matter. *ApJ*. 1985 May;292:371–394.
- [19] Lynden-Bell D. Statistical mechanics of violent relaxation in stellar systems. *MNRAS*. 1967;136:101–+.
- [20] Press WH, Schechter P. Formation of Galaxies and Clusters of Galaxies by Self-Similar Gravitational Condensation. *ApJ*. 1974 Feb;187:425–438.
- [21] Sheth RK, Mo HJ, Tormen G. Ellipsoidal collapse and an improved model for the number and spatial distribution of dark matter haloes. *MNRAS*. 2001 May;323:1–12.
- [22] Tinker J, Kravtsov AV, Klypin A, et al. Toward a Halo Mass Function for Precision Cosmology: The Limits of Universality. *ApJ*. 2008 Dec;688:709–728.
- [23] Gunn JE, Gott JR III. On the Infall of Matter Into Clusters of Galaxies and Some Effects on Their Evolution. *ApJ*. 1972 Aug;176:1.
- [24] Carroll SM, Press WH, Turner EL. The cosmological constant. *ARA&A*. 1992;30:499–542.
- [25] Osterbrock DE, Ferland GJ. *Astrophysics of gaseous nebulae and active galactic nuclei*. ; 2006.
- [26] Strömgren B. The Physical State of Interstellar Hydrogen. *ApJ*. 1939 May;89:526–+.
- [27] Spitzer L. Physical processes in the interstellar medium. ; 1978.
- [28] Shapiro PR. Cosmological H II regions and the photoionization of the intergalactic medium. *PASP*. 1986 Oct;98:1014–1017.
- [29] Shapiro PR, Kang H. Hydrogen molecules and the radiative cooling of pregalactic shocks. *ApJ*. 1987 Jul;318:32–65.
- [30] Davé R, Cen R, Ostriker JP, et al. Baryons in the Warm-Hot Intergalactic Medium. *ApJ*. 2001 May;552:473–483.
- [31] Haardt F, Madau P. Radiative Transfer in a Clumpy Universe. IV. New Synthesis Models of the Cosmic UV/X-Ray Background. *ApJ*. 2012 Feb;746:125.
- [32] Gnedin NY. Effect of Reionization on Structure Formation in the Universe. *ApJ*. 2000 Oct;542:535–541.
- [33] Meiksin A, Madau P. On the photoionization of the intergalactic medium by quasars at high redshift. *ApJ*. 1993 Jul;412:34–55.
- [34] Tselikhovich D, Hirata C. Relative velocity of dark matter and baryonic fluids and the

- formation of the first structures. *Phys. Rev. D*. 2010 Oct;82(8):083520.
- [35] Peebles PJE. *Principles of Physical Cosmology*. ; 1993.
 - [36] Barkana R, Loeb A. In the beginning: the first sources of light and the reionization of the universe. *Phys. Rep.*. 2001 Jul;349:125–238.
 - [37] Gnedin NY, Hui L. Probing the Universe with the Ly α forest - I. Hydrodynamics of the low-density intergalactic medium. *MNRAS*. 1998 May;296:44–55.
 - [38] Bromm V, Ferrara A, Coppi PS, et al. The fragmentation of pre-enriched primordial objects. *MNRAS*. 2001 Dec;328:969–976.
 - [39] Abel T, Bryan GL, Norman ML. The Formation of the First Star in the Universe. *Science*. 2002 Jan;295:93–98.
 - [40] Stecher TP, Williams DA. Photodestruction of Hydrogen Molecules in H I Regions. *ApJ*. 1967 Jul;149:L29.
 - [41] Machacek ME, Bryan GL, Abel T. Simulations of Pregalactic Structure Formation with Radiative Feedback. *ApJ*. 2001 Feb;548:509–521.
 - [42] O’Leary RM, McQuinn M. The Formation of the First Cosmic Structures and the Physics of the $z \sim 20$ Universe. *ApJ*. 2012 Nov;760:4.
 - [43] Wise JH, Turk MJ, Norman ML, et al. The Birth of a Galaxy: Primordial Metal Enrichment and Stellar Populations. *ApJ*. 2012 Jan;745:50.
 - [44] Hirano S, Hosokawa T, Yoshida N, et al. Primordial star formation under the influence of far ultraviolet radiation: 1540 cosmological haloes and the stellar mass distribution. *MNRAS*. 2015 Mar;448:568–587.
 - [45] Turk MJ, Abel T, O’Shea B. The Formation of Population III Binaries from Cosmological Initial Conditions. *Science*. 2009 Jul;325:601–.
 - [46] Greif TH, Bromm V, Clark PC, et al. Formation and evolution of primordial protostellar systems. *MNRAS*. 2012 Jul;424:399–415.
 - [47] Schaerer D. On the properties of massive Population III stars and metal-free stellar populations. *A&A*. 2002 Jan;382:28–42.
 - [48] Alvarez MA, Bromm V, Shapiro PR. The H II Region of the First Star. *ApJ*. 2006 Mar;639:621–632.
 - [49] Kimm T, Cen R. Escape Fraction of Ionizing Photons during Reionization: Effects due to Supernova Feedback and Runaway OB Stars. *ApJ*. 2014 Jun;788:121.
 - [50] Kimm T, Katz H, Haehnelt M, et al. Feedback-regulated escape of LyC photons from mini-haloes during reionisation. *ArXiv e-prints*. 2016 Aug;.
 - [51] Xu H, Wise JH, Norman ML, et al. Galaxy Properties and UV Escape Fractions during the Epoch of Reionization: Results from the Renaissance Simulations. *ApJ*. 2016 Dec;833:84.
 - [52] Wise JH, Demchenko VG, Halicek MT, et al. The birth of a galaxy - III. Propelling reionization with the faintest galaxies. *MNRAS*. 2014 Aug;442:2560–2579.
 - [53] Robertson BE, Furlanetto SR, Schneider E, et al. New Constraints on Cosmic Reionization from the 2012 Hubble Ultra Deep Field Campaign. *ApJ*. 2013 May;768:71.
 - [54] Ma X, Kasen D, Hopkins PF, et al. The difficulty of getting high escape fractions of ionizing photons from high-redshift galaxies: a view from the FIRE cosmological simulations. *MNRAS*. 2015 Oct;453:960–975.
 - [55] Mesinger A, Ferrara A, Spiegel DS. Signatures of X-rays in the early Universe. *MNRAS*. 2013 May;431:621–637.
 - [56] Mitsuda K, Inoue H, Koyama K, et al. Energy spectra of low-mass binary X-ray sources observed from TENMA. *PASJ*. 1984;36:741–759.
 - [57] Xu H, Ahn K, Wise JH, et al. Heating the Intergalactic Medium by X-Rays from Population III Binaries in High-redshift Galaxies. *ApJ*. 2014 Aug;791:110.
 - [58] Ahn K, Xu H, Norman ML, et al. Spatially Extended 21 cm Signal from Strongly Clustered Uv and X-Ray Sources in the Early Universe. *ApJ*. 2015 Mar;802:8.
 - [59] Fan X, Strauss MA, Becker RH, et al. Constraining the Evolution of the Ionizing Background and the Epoch of Reionization with $z \sim 6$ Quasars. II. A Sample of 19 Quasars. *AJ*. 2006 Jul;132:117–136.

- [60] Alvarez MA, Wise JH, Abel T. Accretion onto the First Stellar-Mass Black Holes. *ApJ*. 2009 Aug;701:L133–L137.
- [61] Greig B, Mesinger A, Haiman Z, et al. Are we witnessing the epoch of reionisation at $z = 7.1$ from the spectrum of J1120+0641? *ArXiv e-prints* (160600441). 2016 Jun;.
- [62] Becker GD, Bolton JS, Madau P, et al. Evidence of patchy hydrogen reionization from an extreme Ly α trough below redshift six. *MNRAS*. 2015 Mar;447:3402–3419.
- [63] Planck Collaboration, Adam R, Aghanim N, et al. Planck intermediate results. XLVII. Planck constraints on reionization history. *A&A*. 2016 Dec;596:A108.
- [64] Planck Collaboration, Aghanim N, Ashdown M, et al. Planck intermediate results. XLVI. Reduction of large-scale systematic effects in HFI polarization maps and estimation of the reionization optical depth. *A&A*. 2016 Dec;596:A107.
- [65] Sunyaev RA, Zeldovich YB. The Observations of Relic Radiation as a Test of the Nature of X-Ray Radiation from the Clusters of Galaxies. *Comments on Astrophysics and Space Physics*. 1972 Nov;4:173.
- [66] Santos MR. The High-Redshift Formation of Metal-Poor Globular Cluster Systems. In: Kissler-Patig M, editor. *Extragalactic Globular Cluster Systems*; 2003. p. 348.
- [67] McQuinn M, Furlanetto SR, Hernquist L, et al. The Kinetic Sunyaev-Zel’dovich Effect from Reionization. *ApJ*. 2005 Sep;630:643–656.
- [68] Trac HY, Gnedin NY. Computer Simulations of Cosmic Reionization. *Advanced Science Letters*. 2011 Feb;4:228–243.
- [69] Mesinger A, McQuinn M, Spergel DN. The kinetic Sunyaev-Zel’dovich signal from inhomogeneous reionization: a parameter space study. *MNRAS*. 2012 May;422:1403–1417.
- [70] Zahn O, Reichardt CL, Shaw L, et al. Cosmic Microwave Background Constraints on the Duration and Timing of Reionization from the South Pole Telescope. *ApJ*. 2012 Sep;756:65.
- [71] Songaila A. The Evolution of the Intergalactic Medium Transmission to Redshift 6. *AJ*. 2004 May;127:2598–2603.
- [72] Mesinger A. Was reionization complete by $z \sim 5$ -6? *MNRAS*. 2010 Sep;407:1328–1337.
- [73] Greig B, Mesinger A. The Global History of Reionisation. *ArXiv e-prints* (160505374). 2016 May;.
- [74] McDonald P, Miralda-Escudé J, Rauch M, et al. A Measurement of the Temperature-Density Relation in the Intergalactic Medium Using a New Ly α Absorption-Line Fitting Method. *ApJ*. 2001 Nov;562:52–75.
- [75] York DG, Adelman J, Anderson JE Jr, et al. The Sloan Digital Sky Survey: Technical Summary. *AJ*. 2000 Sep;120:1579–1587.
- [76] Becker GD, Bolton JS. New measurements of the ionizing ultraviolet background over $2 < z < 5$ and implications for hydrogen reionization. *MNRAS*. 2013 Dec;436:1023–1039.
- [77] Miralda-Escudé J, Rees MJ. Reionization and thermal evolution of a photoionized intergalactic medium. *MNRAS*. 1994 Jan;266:343–352.
- [78] Schaye J, Theuns T, Rauch M, et al. The thermal history of the intergalactic medium*. *MNRAS*. 2000 Nov;318:817–826.
- [79] Hui L, Gnedin NY. Equation of state of the photoionized intergalactic medium. *MNRAS*. 1997 Nov;292:27.
- [80] Bolton JS, Becker GD, Wyithe JSB, et al. A first direct measurement of the intergalactic medium temperature around a quasar at $z = 6$. *MNRAS*. 2010 Jul;406:612–625.
- [81] Bolton JS, Becker GD, Raskutti S, et al. Improved measurements of the intergalactic medium temperature around quasars: possible evidence for the initial stages of He II reionization at $z \simeq 6$. *MNRAS*. 2012 Feb;419:2880–2892.
- [82] Ewen HI, Purcell EM. Observation of a Line in the Galactic Radio Spectrum: Radiation from Galactic Hydrogen at 1,420 Mc./sec. *Nature*. 1951 Sep;168:356.
- [83] Muller CA, Oort JH. Observation of a Line in the Galactic Radio Spectrum: The Interstellar Hydrogen Line at 1,420 Mc./sec., and an Estimate of Galactic Rotation. *Nature*. 1951 Sep;168:357–358.

- [84] Scott D, Rees MJ. The 21-cm line at high redshift: a diagnostic for the origin of large scale structure. *MNRAS*. 1990 Dec;247:510.
- [85] Wouthuysen SA. On the excitation mechanism of the 21-cm (radio-frequency) interstellar hydrogen emission line. *AJ*. 1952;57:31–32.
- [86] Field GB. Excitation of the Hydrogen 21-CM Line. *Proceedings of the IRE*. 1958 Jan; 46:240–250.
- [87] Madau P, Meiksin A, Rees MJ. 21 Centimeter Tomography of the Intergalactic Medium at High Redshift. *ApJ*. 1997 Feb;475:429–444.
- [88] Parsons AR, Backer DC, Foster GS, et al. The Precision Array for Probing the Epoch of Re-ionization: Eight Station Results. *AJ*. 2010 Apr;139:1468–1480.
- [89] van Haarlem MP, Wise MW, Gunst AW, et al. LOFAR: The LOw-Frequency ARray. *A&A*. 2013 Aug;556:A2.
- [90] Bowman JD, Cairns I, Kaplan DL, et al. Science with the Murchison Widefield Array. *PASA*. 2013 Apr;30:e031.
- [91] Neben AR, Bradley RF, Hewitt JN, et al. The Hydrogen Epoch of Reionization Array Dish. I. Beam Pattern Measurements and Science Implications. *ApJ*. 2016 Aug;826:199.
- [92] Dewdney PE, Hall PJ, Schilizzi RT, et al. The square kilometre array. *Proceedings of the IEEE*. 2009;97(8):1482–1496.
- [93] Kashikawa N, Ishizaki Y, Willott CJ, et al. The Subaru High- z Quasar Survey: Discovery of Faint $z \sim 6$ Quasars. *ApJ*. 2015 Jan;798:28.
- [94] Willott CJ, Albert L, Arzoumanian D, et al. Eddington-limited Accretion and the Black Hole Mass Function at Redshift 6. *AJ*. 2010 Aug;140:546–560.
- [95] Grissom RL, Ballantyne DR, Wise JH. On the contribution of active galactic nuclei to reionization. *A&A*. 2014 Jan;561:A90.
- [96] Madau P, Haardt F. Cosmic Reionization after Planck: Could Quasars Do It All? *ApJ*. 2015 Nov;813:L8.
- [97] Ellis RS, McLure RJ, Dunlop JS, et al. The Abundance of Star-forming Galaxies in the Redshift Range 8.5–12: New Results from the 2012 Hubble Ultra Deep Field Campaign. *ApJ*. 2013 Jan;763:L7.
- [98] Coe D, Bradley L, Zitrin A. Frontier Fields: High-redshift Predictions and Early Results. *ApJ*. 2015 Feb;800:84.
- [99] Laporte N, Infante L, Troncoso Iribarren P, et al. Young Galaxy Candidates in the Hubble Frontier Fields. III. MACS J0717.5+3745. *ApJ*. 2016 Apr;820:98.
- [100] Oesch PA, Brammer G, van Dokkum PG, et al. A Remarkably Luminous Galaxy at $z=11.1$ Measured with Hubble Space Telescope Grism Spectroscopy. *ApJ*. 2016 Mar; 819:129.
- [101] Schechter P. An analytic expression for the luminosity function for galaxies. *ApJ*. 1976 Jan;203:297–306.
- [102] McLure RJ, Dunlop JS, Bowler RAA, et al. A new multifield determination of the galaxy luminosity function at $z = 7-9$ incorporating the 2012 Hubble Ultra-Deep Field imaging. *MNRAS*. 2013 Jul;432:2696–2716.
- [103] Livermore RC, Finkelstein SL, Lotz JM. Directly Observing the Galaxies Likely Responsible for Reionization. *ArXiv e-prints* (160406799). 2016 Apr.
- [104] Bouwens RJ, Oesch PA, Illingworth GD, et al. The $z \sim 6$ Luminosity Function Fainter than -15 mag from the Hubble Frontier Fields: The Impact of Magnification Uncertainties. *ArXiv e-prints*. 2016 Oct.
- [105] Finkelstein SL, Papovich C, Ryan RE, et al. CANDELS: The Contribution of the Observed Galaxy Population to Cosmic Reionization. *ApJ*. 2012 Oct;758:93.
- [106] Siana B, Shapley AE, Kulas KR, et al. A Deep Hubble Space Telescope and Keck Search for Definitive Identification of Lyman Continuum Emitters at $z \sim 3.1$. *ApJ*. 2015 May; 804:17.
- [107] Nestor DB, Shapley AE, Kornei KA, et al. A Refined Estimate of the Ionizing Emissivity from Galaxies at $z \sim 3$: Spectroscopic Follow-up in the SSA22a Field. *ApJ*. 2013 Mar; 765:47.

- [108] Cooke J, Ryan-Weber EV, Garel T, et al. Lyman-continuum galaxies and the escape fraction of Lyman-break galaxies. *MNRAS*. 2014 Jun;441:837–851.
- [109] Stark DP, Ellis RS, Ouchi M. Keck Spectroscopy of Faint $3 < z < 7$ Lyman Break Galaxies: A High Fraction of Line Emitters at Redshift Six. *ApJ*. 2011 Feb;728:L2.
- [110] Song M, Finkelstein SL, Livermore RC, et al. Keck/MOSFIRE Spectroscopy of $z = 7-8$ Galaxies: $\text{Ly}\alpha$ Emission from a Galaxy at $z = 7.66$. *ApJ*. 2016 Aug;826:113.
- [111] Dijkstra M, Wyithe S, Haiman Z, et al. Evolution in the escape fraction of ionizing photons and the decline in strong $\text{Ly}\alpha$ emission from $z > 6$ galaxies. *MNRAS*. 2014 Jun;440:3309–3316.
- [112] Mesinger A, Aykutalp A, Vanzella E, et al. Can the intergalactic medium cause a rapid drop in $\text{Ly}\alpha$ emission at $z > 6$? *MNRAS*. 2015 Jan;446:566–577.
- [113] Furlanetto SR. The global 21-centimeter background from high redshifts. *MNRAS*. 2006 Sep;371:867–878.
- [114] McQuinn M, Lidz A, Zahn O, et al. The morphology of HII regions during reionization. *MNRAS*. 2007 May;377:1043–1063.
- [115] Kuhlen M, Faucher-Giguère CA. Concordance models of reionization: implications for faint galaxies and escape fraction evolution. *MNRAS*. 2012 Jun;423:862–876.
- [116] Finkelstein SL, Ryan RE Jr, Papovich C, et al. The Evolution of the Galaxy Rest-frame Ultraviolet Luminosity Function over the First Two Billion Years. *ApJ*. 2015 Sep;810:71.
- [117] Arons J, McCray R. Photo-Ionization of Intergalactic Hydrogen by Quasars. *Astrophys. Lett.* 1970;5:123.
- [118] Pawlik AH, Schaye J, van Scherpenzeel E. Keeping the Universe ionized: photoheating and the clumping factor of the high-redshift intergalactic medium. *MNRAS*. 2009 Apr;394:1812–1824.
- [119] So GC, Norman ML, Reynolds DR, et al. Fully Coupled Simulation of Cosmic Reionization. II. Recombinations, Clumping Factors, and the Photon Budget for Reionization. *ApJ*. 2014 Jul;789:149.
- [120] Finlator K, Oh SP, Özel F, et al. Gas clumping in self-consistent reionization models. *MNRAS*. 2012 Dec;427:2464–2479.
- [121] Madau P, Haardt F, Rees MJ. Radiative Transfer in a Clumpy Universe. III. The Nature of Cosmological Ionizing Sources. *ApJ*. 1999 Apr;514:648–659.
- [122] Robertson BE, Ellis RS, Furlanetto SR, et al. Cosmic Reionization and Early Star-forming Galaxies: A Joint Analysis of New Constraints from Planck and the Hubble Space Telescope. *ApJ*. 2015 Apr;802:L19.
- [123] Alvarez MA, Finlator K, Trenti M. Constraints on the Ionizing Efficiency of the First Galaxies. *ApJ*. 2012 Nov;759:L38.
- [124] Chen P, Wise JH, Norman ML, et al. Scaling Relations for Galaxies Prior to Reionization. *ApJ*. 2014 Nov;795:144.
- [125] Benson AJ, Sugiyama N, Nusser A, et al. The epoch of reionization. *MNRAS*. 2006 Jul;369:1055–1080.
- [126] Furlanetto SR, Zaldarriaga M, Hernquist L. The Growth of H II Regions During Reionization. *ApJ*. 2004 Sep;613:1–15.
- [127] Zahn O, Lidz A, McQuinn M, et al. Simulations and Analytic Calculations of Bubble Growth during Hydrogen Reionization. *ApJ*. 2007 Jan;654:12–26.
- [128] Mesinger A, Furlanetto S. Efficient Simulations of Early Structure Formation and Reionization. *ApJ*. 2007 Nov;669:663–675.
- [129] Gnedin NY, Ostriker JP. Reionization of the Universe and the Early Production of Metals. *ApJ*. 1997 Sep;486:581–+.
- [130] Iliiev IT, Mellema G, Ahn K, et al. Simulating cosmic reionization: how large a volume is large enough? *MNRAS*. 2014 Mar;439:725–743.
- [131] Auer LH, Mihalas D. On the use of variable Eddington factors in non-LTE stellar atmospheres computations. *MNRAS*. 1970;149:65–+.
- [132] Davis SW, Stone JM, Jiang YF. A Radiation Transfer Solver for Athena Using Short Characteristics. *ApJS*. 2012 Mar;199:9.

- [133] Finlator K, Özel F, Davé R. A new moment method for continuum radiative transfer in cosmological re-ionization. *MNRAS*. 2009 Mar;393:1090–1106.
- [134] Gnedin NY, Abel T. Multi-dimensional cosmological radiative transfer with a Variable Eddington Tensor formalism. *New A*. 2001 Oct;6:437–455.
- [135] Jiang YF, Stone JM, Davis SW. An Algorithm for Radiation Magnetohydrodynamics Based on Solving the Time-dependent Transfer Equation. *ApJS*. 2014 Jul;213:7.
- [136] Rosdahl J, Teyssier R. A scheme for radiation pressure and photon diffusion with the M1 closure in RAMSES-RT. *MNRAS*. 2015 Jun;449:4380–4403.
- [137] Aubert D, Deparis N, Ocvirk P. EMMA: an adaptive mesh refinement cosmological simulation code with radiative transfer. *MNRAS*. 2015 Nov;454:1012–1037.
- [138] Whalen D, Norman ML. A Multistep Algorithm for the Radiation Hydrodynamical Transport of Cosmological Ionization Fronts and Ionized Flows. *ApJS*. 2006 Feb; 162:281–303.
- [139] Krumholz MR, Klein RI, McKee CF. Radiation-Hydrodynamic Simulations of Collapse and Fragmentation in Massive Protostellar Cores. *ApJ*. 2007 Feb;656:959–979.
- [140] Wise JH, Abel T. ENZO+MORAY: radiation hydrodynamics adaptive mesh refinement simulations with adaptive ray tracing. *MNRAS*. 2011 Jul;414:3458–3491.
- [141] Susa H. Smoothed Particle Hydrodynamics Coupled with Radiation Transfer. *PASJ*. 2006 Apr;58:445–460.
- [142] Pawlik AH, Schaye J. TRAPHIC - radiative transfer for smoothed particle hydrodynamics simulations. *MNRAS*. 2008 Sep;389:651–677.
- [143] Hasegawa K, Umemura M, Susa H. Radiative regulation of Population III star formation. *MNRAS*. 2009 May;395:1280–1286.
- [144] Smith BD, Bryan GL, Glover SCO, et al. Grackle: a Chemistry and Cooling Library for Astrophysics. *ArXiv e-prints* (161009591). 2016 Oct;.